Singularities, structures, and scaling in deformed *m*-dimensional elastic manifolds

B. A. DiDonna* and T. A. Witten
Department of Physics, University of Chicago, Chicago, Illinois 60637

S. C. Venkataramani
Department of Mathematics, University of Chicago, Chicago, Illinois 60637

E. M. Kramer
Department of Natural Sciences and Mathematics, Simon's Rock College, Great Barrington, Massachusetts 01230
(Received 22 December 2000; published 17 December 2001)

The crumpling of a thin sheet can be understood as the condensation of elastic energy into a network of ridges that meet in vertices. Elastic energy condensation should occur in response to compressive strain in elastic objects of any dimension greater than 1. We study elastic energy condensation numerically in two-dimensional elastic sheets embedded in spatial dimensions three or four and three-dimensional elastic sheets embedded in spatial dimensions four and higher. We represent a sheet as a lattice of nodes with an appropriate energy functional to impart stretching and bending rigidity. Minimum energy configurations are found for several different sets of boundary conditions. We observe two distinct behaviors of local energy density falloff away from singular points, which we identify as cone scaling or ridge scaling. Using this analysis, we demonstrate that there are marked differences in the forms of energy condensation depending on the embedding dimension.

DOI: 10.1103/PhysRevE.65.016603 PACS number(s): 46.25.−y, 68.60.Bs, 02.40.Xx, 62.20.Dc

I. INTRODUCTION

In the last several years, there has been a marked interest in the nature of crumpling [1–11]. Field theories have been formulated for the crumpling transition [1], quantitative laws have been deduced for the energy scaling of crumpled sheets [3,4,6], and dynamics of the crumpling process have been simulated and measured [7]. In this paper, we treat crumpling as an example of energy condensation.

The crumpling of a thin elastic sheet can be viewed as the condensation of elastic energy onto a network of point vertices and folding ridges. These structures spontaneously emerge, for example, when a thin sheet of thickness h and spatial extent $L \gg h$ is confined within a ball of diameter $X < L$. For $X \leqslant L/2$ the important length scales become h and X. The elastic energy scaling of vertices and ridges are well understood [3,6]. In the limit $h/X \to 0$, the elastic energy is believed to condense into a vanishingly small area around the ridges and vertices.

There is a significant body of physics literature on energy condensation, because it is a pervasive feature of condensed matter. This behavior is seen in many systems including type-two superconductors [12], strongly turbulent flow [13] as well as in mechanical [14] and electrical [15] material failure. Analogous condensation also occurs in particle-confining gauge field theories [16]. In a mathematical context, such condensation often arises in singular perturbations of nonconvex variational problems [17,18]. A few examples of such problems are the gradient theory of phase transitions [19], wherein the bulk of the energy is condensed into a small neighborhood of the interface between the two phases; Ginzburg-Landau vortices [20] which, among other things, describe type-two superconductors; and solid-solid phase transitions in crystalline materials (martensitic phases) [17,21].

One distinctive aspect of the energy condensation in crumpling is the interesting dependence of the total energy scaling on boundary conditions. A survey of the elastic energy scaling with thickness h for a given material with two-dimensional strain modulus μ illustrates this point. For elastic sheets that are forced so that they form a single conical vertex or "d-cone" [4], the only curvature singularity in the $h \to 0$ limit is at the vertex of the cone [4,9,10]. The total energy of the sheet scales as $\mu h^2 \ln(X/h)$ [10] in this situation. When the boundary conditions are such that there are many vertices and ridges (e.g., confinement), the elastic energy is concentrated on the ridges. For confined sheets, the typical ridge length is on the order of the confining diameter X. It has been argued that ridges with length X have a characteristic total elastic energy that scales as $\mu h^{5/3} X^{1/3}$ [22,23], and that the total energy of the system scales with the same exponent. A final example is the delamination and blistering of thin films, which is described by the same energy functional as the crumpled sheet but with different boundary conditions [24–32]. In this circumstance, the sheet develops a self-similar network of folding lines, whose lengths grow smaller as we approach the boundary [31,32], and the total energy of the sheet scales as μh (with a finite fraction of the energy concentrating in a narrow layer near the boundary, of a width that also scales as h [32]).

Thus, by varying the boundary conditions, the same energy functional can lead to significantly different forms of energy condensation, with different energy scalings and different types of energy bearing structures. This behavior is

*Present address: Department of Physics and Astronomy, University of Pennsylvania, Philadelphia, PA 19104.

contrary to the widely held view that singularities are ''local'' phenomena. Our goal is to study this phenomenon, with a hope of understanding the factors that determine the nature of energy condensation in general systems. In this paper, we study elastic energy condensation in spatial dimensions above three. Our motivation is to understand how the scaling behavior of crumpled sheets and the topology of energy condensation networks generalize for m-dimensional elastic manifolds in d-dimensional space. To this end, our numerical study explores energy condensation in two-sheets in three or four dimensions and three-sheets in dimensions $4-6$, subject to boundary conditions which are akin to confinement.

Our previous work [33,34] showed that the notion of an elastic membrane extends naturally to different dimensions. Such membranes have an energy cost for ''stretching'' deformations that change distances between points in the m-dimensional manifold and have an additional cost for bending into the embedding space. When these costs are isotropic, the material properties may be expressed in terms of a stretching modulus, a bending stiffness, and a''Poisson's ratio'' of order unity. As in two-dimensional manifolds, the ratio of bending stiffness to stretching modulus yields a characteristic length. Indeed, if the manifold is a thin sheet of isotropic d-dimensional material, the thickness h of the sheet is a numerical multiple of the square root of the modulus ratio that may be readily calculated [33].

Our previous paper [35] identified two regimes of dimensionality with qualitatively different response to spatial confinement. The authors considered an elastic m-dimensional ball of diameter L geometrically confined within d-spheres of diameter less than $L/2$. When the embedding dimension d is twice the manifold dimension m or more, the state of lowest energy is one of nonsingular curvature, with stretching elastic energy indefinitely smaller than bending energy. For the complementary cases where d is smaller than $2m$, the deformation is qualitatively different. Such manifolds cannot be geometrically confined in a sphere of diameter smaller than $L/2$ without stretching or singular curvature. In ordinary two-sheets ($m=2$) in three dimensions energy condenses in order to reduce the stretching energy of spatial confinement. The degree of energy condensation depends on the stretching moduli through the thickness h defined above. In three-sheets, singularities or stretching are required in four or five embedding dimensions. Previous work [34] confirmed that for three-sheets confined in four dimensions, energy condenses into a network of linelike vertices and planar ridges. We seek to understand how the degree of energy condensation associated with confinement changes with increasing spatial dimension. We expect that less energy will be required to confine a three-sheet within a five-dimensional sphere than within a four-dimensional sphere, but we do not know *a priori* how the form of energy condensation will differ between these two cases.

We begin our study by giving a brief review of elastic theory in Sec. II. Then, Sec. III quantifies our definitions of ''folding lines'' and ''vertices'' within a framework of isometric embeddings, and in Sec. III A we propose a rule for the topological dimensionality of vertices in energy condensation networks. In Sec. IV, we present analytical estimates for the degree of energy condensation in the crumpled state. Building on existing knowledge, we make predictions for the scaling of energy density with a distance away from the regions of greatest elastic energy. We identify two distinct forms of energy scaling, which we call ridge scaling and cone scaling (the names are based on the geometry these scalings correspond to in ordinary crumpling of two-sheet in three dimensions). Section V describes how we represent elastic manifolds numerically.

Then we present our numerical findings. We begin in Sec. VI with simulations of sheets confined by shrinking hard wall potentials. In this qualitative study, the embedding dimension seems to affect the crumpled structure significantly. The condensation of energy appears to become progressively weaker as the embedding dimension is increased, culminating in no condensation when d reaches $2m$. Numerical difficulties prevented any significant quantitative analysis of the geometrical confinement data. The need for better data motivates the simpler systems we simulated next.

Section VII describes our studies of m-sheets with two disclinations. Disclinations are made by removing wedge shaped sectors from the sheet and then joining the edges of each wedge. The essential feature of a disclination is that it induces the sheet to form a cone, with lines of null curvature converging at a vertex. It has been shown that when *two* disclinations are introduced into a two-sheet in three dimensions, the elastic energy of deformation between the disclinations condenses along a ridge joining the two vertices [3]. These ridges appear completely similar to those in geometrically confined sheets and exhibit the same energy scaling [22]. In our present study, simulated two-sheets in three dimensions formed the familiar ridges, but two-sheets with the same boundary conditions in four-dimensional space had much lower total elastic energies and very different energy distributions. Similarly, three-sheets in 4 spatial dimensions formed ridges closely analogous to those seen in two-sheets, but for three-sheets in five dimensions no ridges were evident. Also, nonparallel disclination lines in three-sheets appear to generate further disclinationlike lines in four spatial dimensions but not in five.

Next, in Sec. VIII we detail our simulations of three-tori allowed to relax in d dimensions. The benefit of this geometry is that we expect it to cause energy condensation without the need to introduce disclinations. Observing that a two-torus cannot be smoothly and isometrically embedded in a space of dimensionality less than four, we expect an elastic sheet with the connectivity of an m-torus embedded in a space of dimension $d<2m$ will relax to a configuration with regions of nonzero strain (condensed into a network of ridges). We found that a three-torus in $d=4$ spontaneously forms a network of planar ridges that intersect in vertex singularities similar to those in the geometrically confined sheets. In $d=5$, the three-torus forms a point-like vertex network with no observable ridges. The energy scaling and presence or absence of ridges mirrored the behavior of sheets with disclinations in Sec. VII. The complexity of the crumpling network decreases with increasing embedding dimension, with spontaneous symmetry breaking evident for d

$=5$. As expected, the elastic energy distribution is homogeneous for $d \geqslant 6$.

Finally, in Sec. IX we present the results of simulations of a ''bow configuration,'' in which the center points of opposite faces of a three-cube were attached and the cube was embedded in four or five spatial dimensions. With proper manipulation of initial conditions, the cube embedded in five dimensions forms a single, pointlike vertex at its center. The energy density scaling away from this singularity agrees with predictions for a novel kind of elastic structure that is a generalization of a simple cone. By contrast, the cube embedded in four dimensions forms a set of linelike vertices and planar ridges that are well modeled by our present understanding of three-dimensional crumpling.

We conclude by discussing the observed energy scaling properties of crumpled elastic sheets. We have developed a means to identify the presence of ridges in m-sheets based solely on their spatial elastic energy distribution. Using the analysis of energy distributions, we demonstrate that folding lines in greater than $m+1$ dimensions have different energy and thickness scaling properties than in $m+1$, but ridges in $m+1$ seem to have the same scaling regardless of m. We found that ridge scaling dominates the crumpling of m-sheets in $m+1$ dimensions, while cone scaling was the only form of scaling witnessed in dimensions greater than $m+1$. Differences in the morphology of higher-dimensional folding lines is discussed briefly. The local structure of these folds is very different from that of the familiar ridges found in two-sheets in three-dimensional space. We also note that our simulational findings strongly support the new rule for the topology of elastic energy bearing structures in higher dimensions, which is presented in Sec. III A. We end with a brief discussion of the mathematical questions raised by the nonlocal character of energy scaling in crumpled sheets.

II. ELASTIC *m*-SHEETS IN *d*-SPACE

In this section, we review the elastic theory of m-sheets in d-space as it is presented in Ref. [33]. In analogy with the elastic two-sheets of everyday experience, an m-sheet in d-dimensional space is an elastically isotropic d-dimensional solid that has a spatial extent of order L in m independent directions and $h \ll L$ in the remaining $d-m$ directions. Specifically, our m-sheet is given by $\mathcal{S} \times B_h^{d-m} \subset \mathbb{R}^d$, where $\mathcal{S} \subset \mathbb{R}^m$ is a set that has a typical linear size L in all directions, and B_h^{d-m} is a $(d-m)$-dimensional ball of diameter h.

We are considering embeddings of the m-sheet in a d-dimensional target space. We first consider the lowest energy embedding in a sufficiently large d-dimensional space, say all of $\mathbb{R}^d$, so that the sheet is not distorted in the embedding. We assume that the undistorted sheet has no intrinsic strains, curvatures or torsions (twists). Since there are no curvatures or torsions, picking an orthogonal basis of $d-m$ vectors for the thin directions at one point on the sheet, and then parallel transporting these vectors to every point on the sheet gives an orthonormal set of basis vectors for every point of the sheet. We can, therefore, describe the geometry of the undistorted sheet, which is a d-dimensional object, by the m-dimensional center surface $\mathcal{S}$ that gives the geometry in the long directions, and the orthonormal basis vectors for the thin directions, that describes the geometry in the thin directions. These basis vectors for the thin directions give a normal frame field to the embedding of the center surface, since they are all orthogonal to each of the long directions in the sheet. Further, since the basis vectors at different points are related by parallel transport in $\mathbf{R}^d$, the normal frame field is torsion free.

For small distortions, we can continue to describe the embedding of the m-sheet by giving the embedding of the center surface $\mathcal{S}$ and by specifying the normal frame field [33]. The rotational invariance in the thin directions implies that the torsion of the sheet in the embedding cannot couple to the geometry of the center surface. Since the sheet has no intrinsic torsion, if there are no applied torsional forces, the normal frame has to remain torsion free. The torsion degrees of freedom, therefore, drop out of the energetic considerations that will determine the geometry of the sheet [33]. Therefore, we can leave out the thin directions and determine the energy of the embedding through an effective Lagrangian that only depends on the long directions, i.e., the geometry of center surface of the sheet $\mathcal{S}$, as embedded in the d-space [33]. This approach puts powerful tools of differential geometry at our disposal. Numerically, this treatment greatly increases the efficiency of our simulations by decreasing the dimension and required grid resolution of our lattice. In the limit $h/L \ll 1$ and for relatively small elastic distortions of the material, this description is highly accurate.

We use Cartesian coordinates in the center surface, which can be viewed as the set $\mathcal{S} \subset \mathbb{R}^m$. We refer to these coordinates as the material coordinates, and quantities referred to the material coordinates will be denoted by Roman subscripts, e.g., i,j,k,l. The configuration of the sheet is given by a vector valued functions $\vec{r}(x_i)$ with values in the d-dimensional target space. We also denote the $d-m$ normal vectors in a choice for an orthonormal, torsion-free frame by $\vec{n}^{(\alpha)}$, with a Greek superscript that takes values $1,2,\ldots,d-m$. Such a choice exists by our previous considerations.

The strain energy density $\mathcal{L}_s$ due to the distortions within the m-sheet is given by the conventional expression [36] in terms of the Lamé coefficients λ and μ,

$$\mathcal{L}_s = \mu \gamma_{ij}^2 + \frac{\lambda}{2} \gamma_{ii}^2, \tag{1}$$

where γ_{ij} is the strain tensor, defined by

$$\gamma_{ij} = \frac{1}{2}\left(\frac{\partial \vec{r}}{\partial x_i} \cdot \frac{\partial \vec{r}}{\partial x_j} - \delta_{ij} \right).$$

The strain tensor quantifies the deviation of the metric tensor of the embedded sheet from its intrinsic metric tensor. Here and henceforth, repeated indices (both Greek and Roman) are summed over all the range of their allowed values.

The nonzero thickness of the m-sheet leads to an energy cost for distortions of the center surface $\mathcal{S}$ in a normal direction, i.e., bending distortions. A measure of the bending of the manifold at any point is the extrinsic curvature tensor

$\vec{\kappa}_{ij}(x_i)$, which is the projection of the second derivatives $\partial_i \partial_j \vec{r}$ into the normal frame. The component of the extrinsic curvature in the normal direction $\vec{n}^{(\alpha)}$ is given by

$$\kappa_{ij}^{(\alpha)} = \frac{\partial^2 \vec{r}}{\partial x_i \partial x_j} \cdot \vec{n}^{(\alpha)}. \tag{2}$$

As shown in Ref. [33], if the strains are small and the curvatures are small compared to $1/h$, the energy density of the bending distortions $\mathcal{L}_b$ is given by

$$\mathcal{L}_b = B\left[\kappa_{ij}^{(\alpha)} \kappa_{ij}^{(\alpha)} + \frac{\lambda}{2\mu} \kappa_{ii}^{(\alpha)} \kappa_{jj}^{(\alpha)} \right]. \tag{3}$$

The bending modulus B in the above equation is determined by the Lamé coefficient μ and the thickness of the sheet h through the relation [33]

$$B = \mu h^2 / \eta(m,d),$$

where $\eta(m,d)$ is given by

$$\eta(m,d) = \frac{d-m}{S_{d-m}} \times \begin{cases} \dfrac{2}{3} & d-m=1 \\ \dfrac{\pi}{4} & d-m=2, \\ \dfrac{1}{d-m+2}\beta(3/2, d-m-2) S_{d-m-1} & d-m>2 \end{cases} \tag{4}$$

where $S_a = 2\pi^{a/2}/\Gamma(a/2)$ is the area of a unit sphere in a dimensions and $\beta(a,b) = \Gamma(a)\Gamma(b)/\Gamma(a+b)$ is the beta function. For $m=3$ and $d=4,5,6$, $\eta(m,d)=3,4$, and 5, respectively.

For studying the geometrical confinement of an elastic m-sheet, the confining forces are assumed to be derived from a potential $V_c(\vec{r})$ in the embedding space. The energy of the m-sheet is the sum of the bending energy, the strain energy, and the energy due to the spatially confining potential. Therefore, the total energy is given in terms of the geometry of the center surface $\mathcal{S}$ by

$$\mathcal{E} = \mu \int_{\mathcal{S}} d^m x \left[\frac{h^2}{\eta} \left(\kappa_{ij}^{(\alpha)} \kappa_{ij}^{(\alpha)} + \frac{\lambda}{2\mu} \kappa_{ii}^{(\alpha)} \kappa_{jj}^{(\alpha)} \right) + \left(\gamma_{ij}^2 + \frac{\lambda}{2\mu} \gamma_{ii}^2 \right) + \frac{V_c(\vec{r}(x_i))}{\mu} \right], \tag{5}$$

where $\eta = \eta(m,d)$ as defined in Eq. (4).

The configuration $\vec{r}(x_i)$ of the sheet in the embedding space is obtained by minimizing the energy $\mathcal{E}$ over the set of all allowed configurations. A (local) minimum energy configuration is obtained by requiring that the variation $\delta\mathcal{E}$ should vanish to the first order for an arbitrary (small) variation $\delta\vec{r}$ of the configuration. Since the energy density contains terms in κ_{ij}, that involve the second derivatives of the function $\vec{r}(x_i)$, the Euler-Lagrange equations for the minimization problem are a system of fourth-order nonlinear elliptic equations on the domain $\mathcal{S}$. Very little is known about the rigorous analysis of such equations. Therefore, we will study the geometrical confinement problem numerically, by approximating the integral in Eq. (5) by a sum over a grid, and minimizing the resulting energy by a conjugate gradient method [37], as we outline below.

Our goal is to study the scaling behavior of the structures on which the energy concentrates as the thickness $h \to 0$. The variational derivative of the potential term is given by

$$\frac{\delta}{\delta \vec{r}} \int_{\mathcal{S}} d^m x V_c(\vec{r}(x_i)) = \nabla_{\vec{r}} V_c(\vec{r}(x_i)).$$

This term leads to a strongly nonlinear coupling between the configuration of the minimizer and the stresses and bending moments in the sheet. Consequently, the conditions for mechanical equilibrium are now ''global'' and the stresses and bending moments determined by the local strains and curvatures should balance a term that depends on the global geometry of the configuration. In addition to complicating the analysis, this introduces length scales besides the thickness h into the problem. This in turn can lead to the lack of simple scaling behavior at equilibrium for the structures in geometrically confined sheets. Note, however, that this is not the case for confinement in a hard wall potential

$$V_c(\vec{r}) = \begin{cases} V_0 & \text{for } \vec{r} \in \Omega \\ +\infty & \text{otherwise,} \end{cases}$$

where Ω is a given set in $\mathbb{R}^d$. The configuration of the minimizer is now restricted to be inside Ω and the gradient of V_c is zero here, so that there is no coupling between the configuration of the minimizer and the stresses and the bending moments in the sheet, in the parts of the sheet that are in the interior of Ω.

One way to get around this problem is to study the configurations where the energy concentration is due to the boundary conditions imposed on the sheet, and not due to an

external potential. If the imposed boundary conditions do not introduce any new length scales, we would then expect to see structures and scalings that are generic, i.e., independent of the precise form of the imposed boundary conditions. This is analogous to the minimal ridge [22] that is obtained by imposing boundary conditions on a two-sheet. Although the minimal ridge is obtained with a specific boundary condition, the scaling behaviors of the ridge are generic and are seen with a variety of boundary conditions.

In this study we first determine the generic structures and scalings that we expect to see for an *m*-sheet in *d*-dimensional space. We also numerically verify our predictions for these scalings by the configuration of an embedded *m*-sheet with a variety of boundary conditions—sheets with disclinations, sheets with a toroidal global connectivity, and sheets in a ''bow'' configuration. In all these cases, the elastic energy is given by

$$\mathcal{E}=\mu\int_{\mathcal{S}} d^m x\left[\frac{h^2}{\eta}\left(\kappa_{ij}^{(\alpha)}\kappa_{ij}^{(\alpha)}+\frac{\lambda}{2\mu}\kappa_{ii}^{(\alpha)}\kappa_{jj}^{(\alpha)}\right)+\left(\gamma_{ij}^2+\frac{\lambda}{2\mu}\gamma_{ii}^2\right)\right]. \tag{6}$$

However, the domain of integration $\mathcal{S}$ is no longer a subset of $\mathbb{R}^m$. It is a domain with singularities in the case of sheets with disclinations or in the ''bow'' configuration, or a set whose global topology is different from $\mathbb{R}^m$, in the case of the sheets with toroidal connectivity. Note that this energy functional is also applicable to the confinement in a hard wall potential, since, without loss of generality, we can set $V_0=0$ for $\vec{r}$ in Ω, and impose the constraint of the hard wall potential through the conditions $\vec{r}(x_i)\in\Omega$ for all $x_i\in\mathcal{S}$. Consequently, the energy is still given by Eq. (6), and the energy condensation is due to the additional constraints that are imposed, that are analogous to the boundary conditions considered above.

We can rewrite the energy using the in-plane stresses σ_{ij} and the bending moments $M_{ij}^{(\alpha)}$ that are conjugate to the strains γ_{ij} and the curvatures $\kappa_{ij}^{(\alpha)}$, respectively. The conjugate fields are given by the variational derivatives

$$\sigma_{ij}=\frac{\delta\mathcal{E}}{\delta\gamma_{ij}}=2\mu\gamma_{ij}+\lambda\delta_{ij}\gamma_{kk}$$

and

$$M_{ij}^{(\alpha)}=\frac{\delta\mathcal{E}}{\delta\kappa_{ij}^{(\alpha)}}=\frac{h^2}{\eta}(2\mu\kappa_{ij}^{(\alpha)}+\lambda\delta_{ij}\kappa_{kk}^{(\alpha)}),$$

where we have taken the variational derivatives as though the fields γ_{ij} and $\kappa_{ij}^{(\alpha)}$ are independent. The energy can now be written as

$$\mathcal{E}=\frac{1}{2}\int_{\mathcal{S}}(M_{ij}^{(\alpha)}\kappa_{ij}^{(\alpha)}+\sigma_{ij}\gamma_{ij})d^m x.$$

Although the energy functional $\mathcal{E}$ does not explicitly couple the strains in the manifolds to the curvatures [see Eq. (6)], they are related by geometric constraints since they are both defined by derivatives of the embedding $\vec{r}(x_i)$. Since the *m*-sheet is intrinsically flat, the Riemann curvature tensor for the embedding of the center surface can be expressed in terms of the *extrinsic* curvature $\kappa_{ij}^{(\alpha)}$ by the Gauss equation [38]

$$R_{ijkl}[\kappa]=\kappa_{ik}^{(\alpha)}\kappa_{jl}^{(\alpha)}-\kappa_{il}^{(\alpha)}\kappa_{jk}^{(\alpha)}.$$

However, the Riemann curvature is intrinsic to the geometry of the center surface, and can be written in terms of the strains as

$$R_{ijkl}[\gamma]=-\gamma_{ik,jl}+\gamma_{il,jk}-\gamma_{jl,ik}+\gamma_{jk,il}+O(\gamma^2).$$

Consequently, the curvatures $\kappa_{ij}^{(\alpha)}$ and the strains γ_{ij} are constrained in order that $R_{ijkl}[\kappa]=R_{ijkl}[\gamma]$.

From the symmetries of the Riemann tensor, it has $m(m-1)(m^2-m+2)/8$ independent components. However, since it can be written purely as a function of the strain γ_{ij}, it can only have as many independent degrees of freedom as the strain itself. As noted in Ref. [33], the strain tensor is symmetric, and further it satisfies *m* additional conditions from the balance of in-plane stresses. Consequently, the strain has $m(m-1)/2$ independent components, and this yields $m(m-1)/2$ independent constraints on the extrinsic curvatures.

For $m=2$, i.e., for two-sheets, there is one constraint, and this is most economically expressed through the Gaussian curvature of the sheet [33]. In terms of the extrinsic curvatures, the Gaussian curvature *G* is given by

$$G[\kappa]=\kappa_{11}^{(\alpha)}\kappa_{22}^{(\alpha)}-\kappa_{12}^{(\alpha)}\kappa_{12}^{(\alpha)},$$

and in terms of the strains, the Gaussian curvature is given by

$$G[\gamma]=-\gamma_{11,22}+2\gamma_{12,12}-\gamma_{22,11}+O(\gamma^2).$$

We can impose the constraint $G[\kappa]=G[\gamma]$ through a Lagrange multiplier χ, so that the augmented energy functional is now given by [33]

$$\mathcal{E}_\chi=\int_{\mathcal{S}} d^m x\left[\frac{1}{2}(M_{ij}^{(\alpha)}\kappa_{ij}^{(\alpha)}+\sigma_{ij}\gamma_{ij})+\chi(G[\gamma]-G[\kappa])\right].$$

Taking the variations with respect to γ_{ij}, χ and $\kappa_{ij}^{(\alpha)}$ give

$$\sigma_{ij}=\delta_{ij}\nabla^2\chi-\partial_i\partial_j\chi\Rightarrow\partial_i\sigma_{ij}=0,$$

$$G[\gamma]=G[\kappa],$$

$$\text{and}\quad \partial_i\partial_j M_{ij}^{(\alpha)}=\sigma_{ij}\kappa_{ij}^{(\alpha)},$$

which are respectively the balance of the in-plane stresses, the Geometric (or First) von Karman equation and the Force (or Second) von Karman equation [33,39]. The first equation also shows that the Lagrange multiplier χ is the scalar stress function of Airy [40].

In this paper, we will mainly focus on the case $m>2$. For $m>2$, an economical way to impose the geometric constraint relating the extrinsic curvatures to the strains is through the Einstein tensor [33]

$$G_{ij}=R_{ikjk}-\frac{1}{2}\delta_{ij}R_{lklk},$$

which has $m(m-1)/2$ independent components since it is symmetric and satisfies the contracted Bianchi identity [41]

$$\partial_i G_{ij}=0.$$

In terms of the extrinsic curvature,

$$G_{ij}[\kappa]=\kappa_{ij}^{(\alpha)}\kappa_{kk}^{(\alpha)}-\kappa_{ik}^{(\alpha)}\kappa_{jk}^{(\alpha)}-\frac{1}{2}\delta_{ij}[\kappa_{ll}^{(\alpha)}\kappa_{kk}^{(\alpha)}-\kappa_{lk}^{(\alpha)}\kappa_{lk}^{(\alpha)}], \tag{7}$$

and to the first order in the strains

$$G_{ij}[\gamma]=-\gamma_{ij,kk}+\gamma_{ik,jk}-\gamma_{kk,ij}+\gamma_{kj,ik}+\delta_{ij}[\gamma_{ll,kk}-\gamma_{lk,lk}]. \tag{8}$$

As in the case $m=2$, the constraint $G_{ij}[\kappa]=G_{ij}[\gamma]$ is incorporated through a tensor Lagrange multiplier χ_{ij}. The augmented energy functional is given by

$$\mathcal{E}_\chi=\int_{\mathcal{S}} d^m x\left[\frac{1}{2}(M_{ij}^{(\alpha)}\kappa_{ij}^{(\alpha)}+\sigma_{ij}\gamma_{ij})+\chi_{ij}(G_{ij}[\gamma]-G_{ij}[\kappa])\right].$$

Taking the variations with respect to γ_{ij}, χ_{ij}, and $\kappa_{ij}^{(\alpha)}$ give the balance of in-plane stresses

$$\partial_i\sigma_{ij}=0,$$

the Geometric von Karman equation

$$G_{ij}[\gamma]=G_{ij}[\kappa], \tag{9}$$

and the Force von-Karman equation

$$\partial_i\partial_j M_{ij}^{(\alpha)}=\sigma_{ij}\kappa_{ij}^{(\alpha)}, \tag{10}$$

respectively [33]. In the case $m=3$, the Lagrange multiplier χ_{ij} is the Maxwell stress function [42].

III. STRUCTURES IN ELASTIC *m*-SHEETS

We will now investigate the minimum energy configurations of the sheet with external forcing. As we discussed earlier, the sheet can be forced either by an external potential $V_c(\vec{r})$ [see Eq. (5)] or by restricting the set of admissible configurations by appropriate boundary conditions [Eq. (6)]. Since confinement by a hard wall potential of radius r_0 is also given by the energy functional in Eq. (6) where the admissibility condition is that $\|\vec{r}(x)\|\leq r_0$ for all $x\in\mathcal{S}$, we will restrict our attention to the energy functional $\mathcal{E}$ in Eq. (6).

From Eq. (6), we see that the only length scales in the energy functional are the thickness h and the length scale L that is associated with the center surface $\mathcal{S}$. Since the effective bending modulus $\mu h^2/\eta$ goes to zero as $h\to 0$, except in the vicinity of regions with large curvature, the large scale $[O(L)]$ behavior of crumpled sheets should be determined almost entirely by the stretching energy functional

$$\mathcal{E}_s=\mu\int_{\mathcal{S}}(\gamma_{ij}^2+c_0\gamma_{ii}^2)d^m x,$$

which penalizes the deviation of the configuration from an isometry. Indeed, crumpled two-sheets in three dimensions can be described as a set of nearly isometric regions bounded by areas of large curvatures that include vertices and boundary layers around folds. Since the curvature in these regions is large, the bending energy in this region will continue to remain relevant as $h\to 0$. As $h\to 0$, the width of, and the strain in, the boundary layer around folds approaches zero, and the only nonisometric regions are the vertices.

For the remainder of this paper we assume that in any dimension, the minimum energy configurations of crumpled *m*-sheets converge in the $h\to 0$ limit to configurations that are locally isometric and have smooth, well-defined curvature almost everywhere. In this view, the regions of elastic energy concentration in the *m*-sheets converge in the $h\to 0$ limit to a *defect set* in the manifold that is not locally smooth and isometric, and this defect set is as small as possible relative to the boundary conditions imposed on the sheet. The limiting procedure that connects the defect set to the energy concentration regions is elaborated upon in Sec. III A.

These assumptions give us descriptive tools to classify the elastic energy structures in higher-dimensional crumpled sheets in terms of well-defined concepts of isometry. More importantly, the identification of crumpling with isometric embedding will allow us to make predictions for the dimensionality of energy condensation regions in *m*-sheets for $m>2$ based on geometric results on isometric immersions. We will present these arguments in Sec. III A and the numerical studies reported in Secs. VII–IX appear to support these predictions.

A. Dimensionality of defects

In this section we define a certain type of singularity called a vertex that must exist in confined *m*-sheets. We then argue that a vertex must have a dimensionality of at least $2m-d-1$. In previous work [35] we showed that a *m*-sheet embedded smoothly and isometrically into a space of dimension less than $2m$ must have straight lines in the sheet material, which extend across the sheet and remain undeformed. Specifically, there exists through any point p at least one straight line in the undistorted *m*-sheet $\mathcal{S}$, which (1) is straight and geodesic in the embedding space $\mathbb{R}^d$, and (2) extends to the boundary of $\mathcal{S}$. We will denote this result as Theorem 1. Theorem 1 implies that a *m*-sheet of minimum diameter L cannot be confined to a *d*-dimensional ball of radius smaller than $L/2$, if $d<2m$, where the minimum diameter L is given by

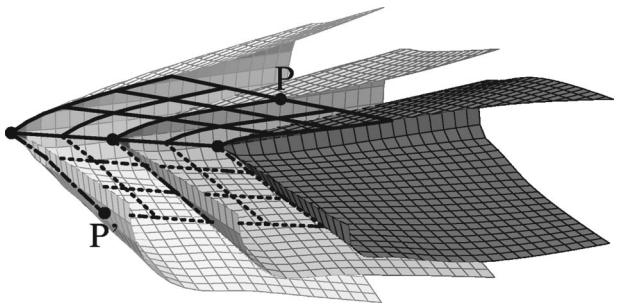

FIG. 1. Flat subspaces R in a crumpled sheet. The figure shows sections of three parallel planes of a thin three-cube confined in four dimensions by boundary conditions discussed in Sec. IX. This sheet is nearly isometric over most of its volume, as anticipated in Sec. III A. The arguments of this section suggest that such sheets should have a nearly-flat two-dimensional subsheet R through any point p. The R for the indicated point p is shown as a solid grid. The nearly flat subsheet R' for a different point p' is shown as a dashed grid. The adjacent boundaries of R and R' meet in a nearly straight, one-dimensional region. We identify this region as a vertex.

$$L = 2 \max_{p \in \mathcal{S}} [\max_{r>0} \{r : B(p,r) \subseteq \mathcal{S}\}],$$

and $B(p,r)$ is the m-dimensional ball of radius r centered on p. By taking points far from the boundary of $\mathcal{S}$, we may identify lines roughly of the size $L/2$ or longer. It is clearly impossible to confine the sheet to a region smaller than such a line.

Observations of embedded sheets and generalizing the proof from Ref. [35] lead us to conjecture the following extension to Theorem 1. We conjecture that through any point p there is a $(2m-d)$-dimensional subsheet [48] R such that

(1) R is totally geodesic in the sheet.

(2) The image of R under the embedding is totally geodesic in $\mathbb{R}^d$. This together with item 1 implies that the sheet is *flat*.

(3) If the point p is a distance X from the boundary of $\mathcal{S}$, then the subsheet R through p contains a $(2m-d)$-dimensional ball of diameter X.

We denote these assertions as Conjecture 1. The subsheets R can be readily identified for a simple cone in a two sheet. For any point p on the cone, R is the half-line extending from the apex through p. Figure 1 illustrates an example of a three-sheet in which the subsheets R are two dimensional.

We may in principle confine an m-sheet isometrically within a ball of arbitrarily small size by removing subsets of $\mathcal{S}$ so that it has ''interior'' boundaries. We shall denote the removed part as the *defect set* $\mathcal{D}$. By removing sufficiently many subsets, we can assure that all points of the resulting sheet $\mathcal{S}'$ are as close to the (interior) boundary as we like. In order that the remaining region be isometric, further conditions are needed: Conjecture 1 forces some of the removed regions to have a dimensionality greater than some limit, as we now show.

We first confine a convex m-sheet $\mathcal{S}$ within a ball of diameter X much smaller than the minimum diameter L of the sheet. As indicated above, this confinement requires strain or singularities. We now remove a defect set $\mathcal{D}$ from the sheet sufficient to allow the remaining sheet $\mathcal{S}'$ to be isometric, as illustrated in Fig. 2. We choose a point p further than X from the original $\mathcal{S}$ boundary, as measured along the sheet. The subsheet R at point p can have a minimum diameter no greater than X; otherwise this flat subspace would not fit into the confining ball. Thus the original boundary of $\mathcal{S}$ cannot touch the boundary of R; R must be bounded everywhere by $\mathcal{D}$. Now, since R is a $(2m-d)$-dimensional set, at least part of its boundary must have dimension at least $(2m-d-1)$. (The boundary may also have additional parts of lower dimension, but we ignore these.) The set $\mathcal{D}$ adjacent to this boundary must have at least this dimension as well. Thus, most R's in the sheet must be bounded over part of their boundary by defect sets $\mathcal{D}$ whose dimension is $(2m-d-1)$ or more.

These defect sets in strictly isometric sheets have implications for the confinement of real elastic sheets. To see this, we repeat the confinement procedure above taking $\mathcal{S}$ to be an elastic sheet of thickness h. We anticipate that regions of concentrated strain will appear, as they do in ordinary crumpled two-sheets. Following the procedure used above, we remove part of $\mathcal{S}$ near the regions of greatest strain, such as the intersection of R and R' in Fig. 1. Specifically, we remove sets of minimum diameter δ, and denote the set of removed points $\mathcal{D}_\delta$. We remove the smallest set such that the remaining sheet $\mathcal{S}'_\delta$ becomes isometric in the limit as $h \to 0$. We now reduce the minimun diameter δ of our set and repeat the procedure. We suppose that the new defect set $\mathcal{D}_\delta$ is a subset of the old one, and that we are led to a well-defined

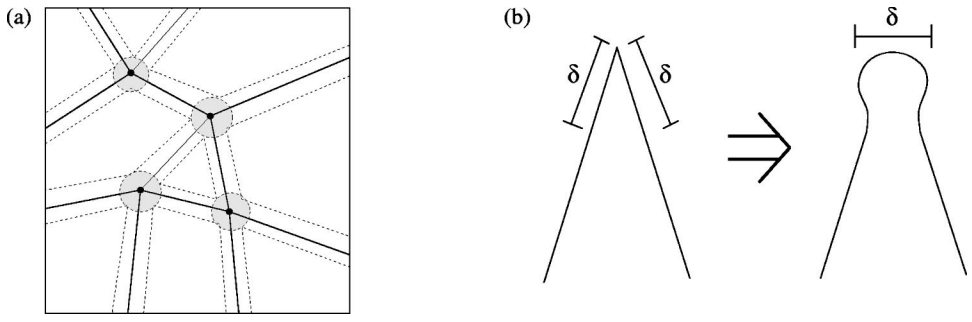

FIG. 2. (a) Illustration of the regions $\mathcal{D}$, $\mathcal{K}$, $\mathcal{D}_\delta$, and $\mathcal{K}_\delta$ for a two-sheet. The points are a possible set $\mathcal{D}$ and the shaded circles are the corresponding $\mathcal{D}_\delta$. The solid lines are a possible set $\mathcal{K}-\mathcal{D}$, and the area within the dashed lines are the corresponding $\mathcal{K}_\delta-\mathcal{D}_\delta$. (b) Illustration of a potential way to soften the folding around a region in $\mathcal{K}$.

limiting set $\mathcal{D}$ as $\delta \to 0$. For each δ we may consider the boundary of R for a given point p. Supposing that this boundary also behaves smoothly, we infer that it retains its dimensionality of at least $2m-d-1$ inferred above. Thus the limiting defect set $\mathcal{D}$ should also have at least this dimension. Returning now to the full elastic sheet $\mathcal{S}$, we expect the strain to be concentrated on the defect set $\mathcal{D}$. The example of Fig. 1 suggests that R sets are bounded by regions of high strain, whose dimension has the minimal value $2m-d-1$. The numerical work in later sections gives more systematic evidence of these strained regions. We shall denote the limiting set $\mathcal{D}$ as the *strain defect set* and denote each connected part of $\mathcal{D}$ as a *vertex*.

Although the elastic sheet $\mathcal{S}'_\delta$ becomes isometric as $h \to 0$, further singularities can develop as $\delta \to 0$. Ordinary two-sheets in three-space show this behavior, as illustrated in Fig. 2. Here the minimal vertex dimension $2m-d-1$ is 0. The set $\mathcal{D}_\delta$ consists of the four shaded disks: each disk constitutes a vertex. Removing these disks permits strain-free confinement to a fraction of the size of the sheet. However, the strain-free deformation develops large curvature as δ becomes small. The diverging curvature is concentrated on lines joining the vertices. Similar diverging curvature must occur in intact sheets as $h \to 0$. We denote such regions by $\mathcal{K}$, which we call the *curvature defect set*. For completeness, we define a set $\mathcal{K}_\delta$ that contains the regions of high curvature around $\mathcal{K}$ for $\delta > 0$. For intact sheets, we expect the strain to be significant in the region $\mathcal{D}$ but very small outside of it—noting that the geometric von Karman equation, Eq. (9), relates large gradients in the strain to large curvature, we conclude that $\mathcal{D}$ must be a subset of $\mathcal{K}$. We denote each connected piece of $\mathcal{K}-\mathcal{D}$ as a *fold* in the crumpled sheet. The relationship between these folds and stretching ridges [23] is discussed in the next section.

Thus far we have considered effects due to confinement in a small ball in $\mathbb{R}^d$. We expect similar effects if we impose other constraints that reduce the spatial extent of the embedded sheet. We expect defect sets $\mathcal{D}$ and $\mathcal{K}$ like those above to form spontaneously here as well. Our numerical investigations reported below do indeed show such behavior. We compare our expectations with the numerical findings in Sec. X.

IV. ENERGY SCALING

We now return to the consideration of sheets with small $h > 0$. We consider sheets that are thin enough that the strains far away from the singular set are much less than $O(1)$. This is the range of thicknesses that is normally considered in the study of thin two-sheets [6,22]. In this range the preferred configuration of a two-sheet is well described by asymptotically matching nearly isometric embedding over most of the sheet to finite boundary layers around the singular set $\mathcal{K}$ (within which the strains and curvatures may become large on the scale of L, the manifold size). We maintain the assumption that energetically preferred embeddings will exhibit near isometry outside the singular set for m-sheets in d-dimensional space, and view the singular set as the subset of the material manifold onto which elastic energy condenses as $h \to 0$. We wish to study the degree of energy condensation onto these elastic structures as a function of the material and embedding dimensions and the elastic thickness h. In this section, we show how the scaling of elastic energy density with volume away from the condensation regions can be used to quantify the degree of energy condensation in crumpled m-sheets. We distinguish two cases for the structures involved in crumpling. In the first case, $\mathcal{K}=\mathcal{D}$ and singular curvature occurs only at vertices. In the complimentary case, $\mathcal{K}-\mathcal{D} \neq \varnothing$, vertices are connected by folds in the $h \to 0$ limit. We show that these two cases have distinctive energy scaling signatures when two-sheets are crumpled in three-dimensions. Anticipated scaling exponents for general crumpling are inferred by analogy to lower-dimensional crumpling.

There are three types of data we may use to analyze minimum energy sheet configurations: the detailed embedding coordinates and the bending and stretching energy densities in the manifold coordinates. To see whether energy has condensed in our simulated sheets, we first identify regions of high energy concentration by plotting surfaces of constant bending or stretching elastic energy in the material coordinates. Figure 3 illustrates, for the case of a two-sheet in three dimensions, how surfaces of constant bending energy highlight the energy-bearing regions of the sheet. We then look at the coordinate information to associate regions of energy concentration with either vertices or folds.

For the remainder of our analysis we consider the energy density data only as a function of volume fraction, independent of position. This removes any ambiguity in defining the center points of the high-strain regions around $\mathcal{D}$, and it provides a natural framework for defining the degree of energy condensation. Let the variable Φ represent the volume fraction in the manifold coordinates measured from the regions of highest to lowest energy density, $0 \leqslant \Phi \leqslant 1$. Thus, Φ can be written as

$$\Phi(\mathcal{L}) = \frac{1}{V_{total}} \int_{\mathcal{L}(\vec{x}') \geqslant \mathcal{L}} d^m x', \tag{11}$$

where $\mathcal{L} = \mathcal{L}_b + \mathcal{L}_s$ is the elastic energy density defined in Eqs. (1) and (3), and

$$V_{total} = \int_{\mathcal{S}} d^m x'.$$

Surfaces of constant energy in the manifold coordinates are also surfaces of constant Φ. Inverting Eq. (11) associates a volume fraction with each observed value of the local elastic energy density. We can write the total energy E in the manifold as

$$E = \int_0^1 d\Phi' \, \mathcal{L}(\Phi'). \tag{12}$$

We say the energy is *condensed* in a volume fraction Φ_c if for $\Phi > \Phi_c$ the energy density $\mathcal{L}$ falls away faster than Φ^{-1}. If this is the case, then the upper limit of integration can be pushed to infinity without changing the value of the integral

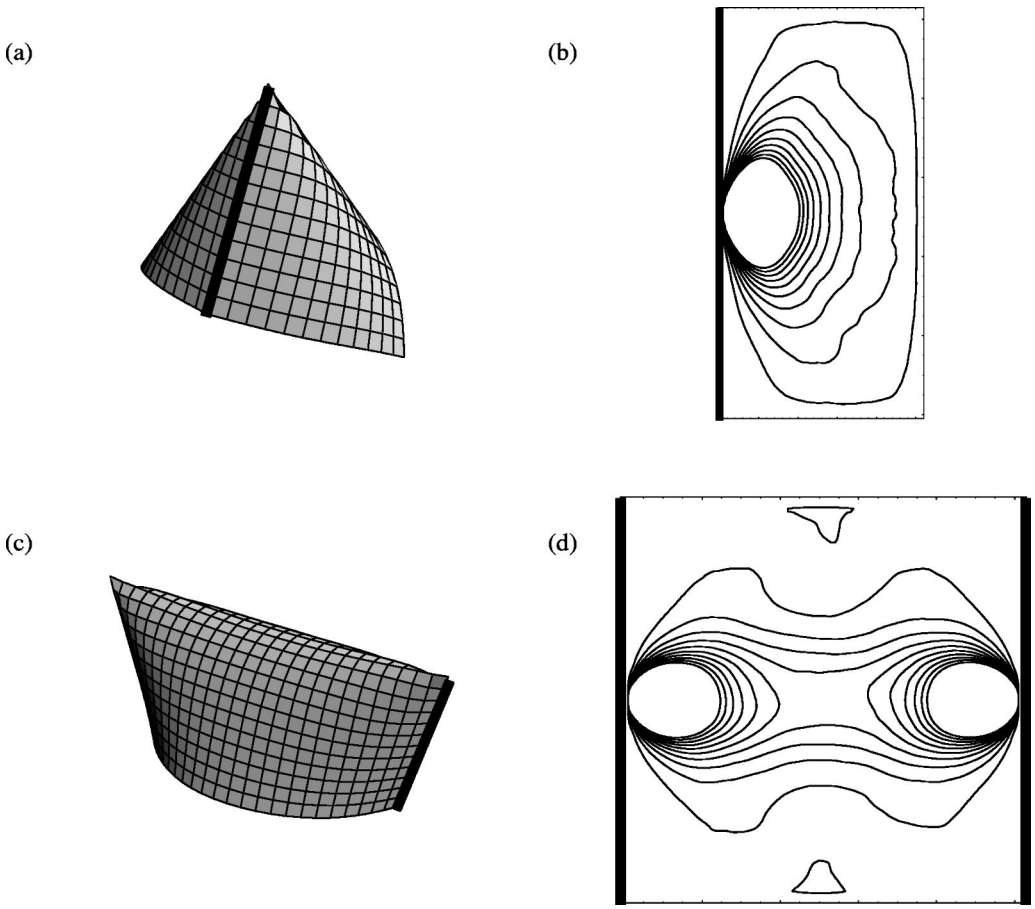

FIG. 3. A cone and a ridge formed with disclinations. Image (a) shows a minimal elastic energy embedding for a two-sheet with one disclination in three-dimensional space. The sheet was 50×100 lattice units in size and had an elastic thickness of $\sim1/100$ in lattice units. The disclination was formed by folding one edge at its center point and attaching the two halves. The minimal energy configuration is a cone. Plot (b) shows surfaces of equal bending energy for the sheet in (a), plotted in its material coordinate system. Image (c) shows a minimal elastic energy embedding for a two-sheet with *two* disclinations in three-dimensional space. The sheet was 100×100 lattice units in size and had an elastic thickness of $\sim1/10$ in lattice units. The minimal energy configuration is a ridge. Plot (d) shows surfaces of equal bending energy for the sheet in (c), plotted in its material coordinate system. In each image, heavy lines indicate edges of the sheet that were joined together to make the disclinations.

by more than a finite fraction. By repeating this analysis for the bending energy $\mathcal{L}_b$ or the stretching energy $\mathcal{L}_s$, we may characterize the condensation of these forms of energy individually.

We may now make predictions for the elastic energy scaling exponents based on our knowledge of the structures found in crumpled sheets. We first consider the case where the set $\mathcal{K}=\mathcal{D}$. In the familiar crumpling of two-sheets in three dimensions $\mathcal{K}=\mathcal{D}$ when the sheet contains a single vertex and the configuration outside the vertex is conical. In any dimension, it is easy to see that far away from $\mathcal{D}$ the conformation should be independent of the small length scale h. Far away from the curvature singularity, there is no intrinsic length scale, so simple dimensional analysis tells us that the curvature must be a numerical multiple of r^{-1}, where r is the distance from the vertex. The preferred embedding is thus a simple generalization of a cone, with straight line generators radiating from a central vertex and transverse curvatures decreasing as $1/r$ along the generators. The cone configuration is isometric outside the vertex for $h=0$, but for $h>0$ it acquires small but finite strain. Dimensional analysis of the force von Karman equation, Eq. (10), for a curvature of the form $C(r,\theta)=g(\theta)/r$ yields strain scaling of the form h^2/r^2 for nearly isometric embeddings. Thus, for energetically preferred embeddings, the bending and stretching energy densities should scale as $1/r^2$ and h^2/r^4, respectively. We can express this energy scaling in terms of the volume fraction Φ by finding how Φ grows with r. In any principal material direction, smooth curvature of order C will typically persist over a length of order $1/C$. In a three-sheet, the volume of high energy density surrounding an energetic cone generator will therefore grow as r^2 if the curvature in one material directions transverse to the generator dominates, or as r^3 if the curvatures in both transverse directions are on the same order. The bending energy density will respectively scale as Φ^{-1} or $\Phi^{-2/3}$. Since the strain along a generator dies twice as quickly as the curvature, the stretching energy density will correspondingly scale as Φ^{-2} or $\Phi^{-4/3}$. Thus we surmise that conical scaling has the typical form

$$\mathcal{L}_b \sim \Phi^{-p}, \qquad \mathcal{L}_s \sim \Phi^{-2p}, \tag{13}$$

where $p=2/(1+n)$, and n is an integer equal to the number of transverse curvature directions along energetic cone generators. In all the geometries accessible to two or three-sheets, the stretching energy is condensed while the bending is not—this is not the case in all higher dimensions, where the value of n can be greater than 3 and the stretching energy not condensed.

We now consider configurations that have $\mathcal{K}-\mathcal{D}\neq\varnothing$. We have denoted each connected piece of $\mathcal{K}-\mathcal{D}$ as a *fold* in the previous section. At this point we need to make a distinction between folds and ridges. For two-sheets in three dimensions with $h>0$, folds have an energetically preferred local structure. We describe folds in this context as ridges, a term that encompasses both the geometric and energetic structure. In general crumpling, we do not know *a priori* whether the local structure around folds will be similar to that in lower-dimensional crumpling, so we must make our definition of a ridge more precise. Since we already have a geometrical descriptor for folds, we use the term ridge to describe a certain kind of energetic structure associated with folds. The generalization of a ridge is a boundary layer around a fold whose energy scaling depends on two length scales—the elastic thickness h of the sheet and the length L of the fold. Clearly, in the thin limit these are the only two length scales that can be important around the fold. Conversely, there must be at least two length scales if there is to be any nontrivial scaling of the ridge profile with thickness h. The presence of two length scales allows for a balance between the coupled bending and stretching energies, which is also a hallmark of ridges (and could be used as an alternative equivalent definition)

For two-sheets in three dimensions, the condition $\mathcal{K}-\mathcal{D}\neq\varnothing$ occurs, e.g., when there are two vertices joined by a ridge, as in Fig. 3. It is well known [22] that the elastic energy density in the region surrounding $\mathcal{K}$ that encompasses a ridge is less than that at vertices (the region surrounding $\mathcal{D}$) but much greater than that in the region of $\mathcal{S}-\mathcal{K}$ away from the energy condensation structures. Ridges begin and end at vertices, with the elastic energy density falling smoothly along the ridge length away from each vertex. This implies that when ridges are present, the scaling of $\mathcal{L}(\Phi)$ at values of Φ much less than 1 but large enough to fully contain the vertices will be determined by the parts of ridges that are closest to vertices. Ridges are also known to have a complicated spatial structure, but we assume that the ridge solution converges to a simple scaling solution near the vertex, where the ridge length should become unimportant. It has been shown [22,23] that the total bending and stretching energy of ridges in two-sheets scale the same way with manifold length scales and obey a virial theorem: the ratio of the total bending to stretching energy is 5–1. The same virial ratio was also demonstrated for $(m-1)$-dimensional ridges in m-sheets [34]. We therefore infer that to lowest order, the bending and stretching energy densities must follow *identical* scaling in the simple scaling region near vertices. The virial relation, $E_b=5\times E_s$, should also be evident in the ratio of scaling prefactors for the two energies. Furthermore, the total elastic energy in a ridge diverges as the length of the ridge becomes infinite [23], so the energy density along the ridge should not fall faster than Φ^{-1}. Thus we expect the scaling behavior of ridges to follow

$$\left.\begin{aligned}\mathcal{L}_b &\sim \Phi^{-q}\\ \mathcal{L}_s &\approx 1/5\,\mathcal{L}_b \sim \Phi^{-q}\end{aligned}\right\} 0<q<1. \tag{14}$$

This dependence implies that strain energy has not condensed onto the vertices alone if ridges are present. In general, our assumption of near-isometry away from the defect set implies that strain will condense out of the bulk of the m-sheet. Thus we expect that the strain must condense onto the ridges and vertices—onto the full set $\mathcal{K}$. This means that, beginning at some $\Phi_c<1$ that marks the boundary of the ridge scaling region, there will be a more rapid dropoff (faster than Φ^{-1}) of strain energy with volume away from the ridges.

We can calculate the anticipated scaling exponent q above based on the anticipated scaling of the ridge width $w(r)$ at a distance r from a vertex, viz $w(r)=w(X)f(r/X)$, where X is the length of the ridge. Previous work [33] shows that $w(X)\sim h(X/h)^{2/3}$ for $(m-1)$-dimensional ridges in m-sheets. We anticipate that $w(r)\ll w(X)$ when $r\ll X$, and that in this regime $w(r)$ is independent of X. Then our scaling assumption implies $w(r)\approx h(r/h)^{2/3}$. The transverse curvature $C(r)$ is as usual presumed to be of order $1/w(r)$. Lobkovsky [22] originally derived this scaling property based on more detailed assumptions. The curvature energy should be significant in a region of width w around the center of the ridge. The local energy density therefore scales as $C^2\sim r^{-4/3}$, while the high-energy volume should grow as $\Phi\sim r\times 1/C=r^{5/3}$. Thus the above curvature scaling leads to $\Phi^{-4/5}$ scaling for both $\mathcal{L}_s$ and $\mathcal{L}_b$ around the vertex if it is the end point of a ridge. This scaling was originally derived for two-sheets embedded in three dimensions. Other work [33] suggests that the same scaling should hold for m-sheets in $(m+1)$-dimensional spaces. For m-sheets, ridges with spatial extent X in l long directions and width of the form $w(x)$ given above in the remaining $m-l$ directions will occupy a total volume $X^m(h/X)^{(m-l)/3}$. Compared with the total volume of the manifold, which is of order X^m, the high-energy volume fraction is $\Phi_c\sim(h/X)^{(m-l)/3}\ll 1$. Thus there is energy condensation onto ridges. For general dimensions, we reason that any balance of bending and stretching energies should lead to a virial relation, and a virial relation in turn implies parallel scaling of the two energy densities. So, Eq. (14) should hold for all higher-dimensional generalizations of ridges.

V. NUMERICAL METHODS

For the present study we have generalized the numerical approach of Seung and Nelson [2], modeling an m-sheet as an m-dimensional rectangular lattice and adding terms to the elastic energy to produce bending stiffness. Properly speaking, we simulate phantom m-sheets, which can pass through

themselves. In the latter part of this section, we discuss the parameter range in which the phantom *m*-sheet behaves like a physical *m*-sheet, as well as the special implications of the phantom approximation on the structure of vertex singularities.

Our manifold is a hypercubic array of nodes labeled by $\underline{I} \equiv \{i_1, \ldots, i_m\}$. Each node has a *d*-dimensional position vector $\vec{r}(\underline{I})$. The relaxed lattice has a nearest-neighbor distance *a*. The lattice displacement from a site at $\underline{I}$ to a nearby one can be expressed by a vector of *m* integers, $\underline{\Delta}$. It is convenient to define the lattice displacements $\vec{u}(\underline{I},\underline{\Delta})$, defined as the displacement between the node at site $\underline{I}$ and the one shifted by $\underline{\Delta}$,

$$\vec{u}(\underline{I},\underline{\Delta}) \equiv -\vec{r}(\underline{I}) + \vec{r}(\underline{I}+\underline{\Delta}). \tag{15}$$

The stretching energy $U(\{\vec{R}\})$ for a three-sheet ($m=3$) is now defined as

$$U \equiv G \sum_{\underline{I}} \sum_{\underline{\Delta}=\mathrm{NN}} (|u(\underline{I},\underline{\Delta})| - a)^2 + c_s \sum_{\underline{I}} \sum_{\underline{\Delta}=\mathrm{NNN}} (|u(\underline{I},\underline{\Delta})| - \sqrt{2}a)^2. \tag{16}$$

Here NN denotes the six nearest-neighbor sites $\underline{\Delta} = (\pm 1,0,0)$, $(0,\pm 1,0)$, and $(0,0,\pm 1)$. The NNN sites are the 12 second neighbor sites of the form $(\pm 1,\pm 1,0)$, etc. The weight coefficient c_s assures that *U* is isotropic, i.e., independent of the direction of strain relative to the lattice. We found by direct calculation of the elastic energy for uniform strain in the (1,0,0), (1,1,0) and (1,1,1) directions, minimized with respect to lateral expansion, that $U[\gamma]$ was equal for the three directions of strain when $c_s = 1$. The corresponding Poisson ratio is 1/4. By expanding Eq. (16) for small deviations of the three-sheet from zero deformation and equating terms with those of Eq. (1), we infer that for our lattice $\mu = 4a^2 G$ and $\lambda = \mu$.

We use a discrete form of Eq. (2) to determine the curvatures in our simulated *m*-sheet. For each origin site $\underline{I}$ we evaluate the diagonal elements $\vec{\kappa}_{ii}$ from the nearest-neighbor separations

$$\vec{\kappa}_{ii} \approx \frac{1}{a^2}\{[\vec{r}(\underline{I}+\underline{\Delta}_i) - \vec{r}(\underline{I})] - [\vec{r}(\underline{I}) - \vec{r}(\underline{I}-\underline{\Delta}_i)]\}. \tag{17}$$

The off-diagonal elements $\vec{\kappa}_{ij}$, $i \neq j$ are computed in a similar fashion from the next nearest-neighbor positions:

$$\vec{\kappa}_{ij} \approx \frac{1}{4a^2}[\{\vec{r}(\underline{I}+\underline{\Delta}_i+\underline{\Delta}_j) - \vec{r}(\underline{I}+\underline{\Delta}_i-\underline{\Delta}_j)\} - \{\vec{r}(\underline{I}-\underline{\Delta}_i+\underline{\Delta}_j) - \vec{r}(\underline{I}-\underline{\Delta}_i-\underline{\Delta}_j)\}]. \tag{18}$$

Once the curvature matrix $\vec{\kappa}$ is known for each site, we may compute the curvature energy E_b from Eq. (3). To save computational time we do not project the curvature vectors onto the normal space of the manifold at $\underline{I}$. This amounts to including tangential components in the curvature tensor defined in Eq. (2). It is the usual practice in linear elasticity to neglect these terms because of their smallness [36], so leaving them in for computational efficiency does not introduce any significant change to the energy density profile.

The sizes and elastic thicknesses of the lattices used in our simulations were arrived at through a trial-and-error balancing of computational resources and data quality. We minimized elastic energy by using an inverse gradient routine, which theoretically converges in $\sim N^2$ steps for a harmonic potential with *N* degrees of freedom [37]. However, experience shows that the convergence becomes much less efficient when we make the elastic sheets very thin, since in this limit the total energy functional is highly nonlinear and has large prefactors for the highest-order terms. This effect in elastic simulations was described in Ref. [43], but their ''reconditioning'' approach to regaining fast convergence requires too much computational overhead to be of use on large three-dimensional lattices. The computational cost of larger lattices must be balanced against the range of validity of the discrete lattice approximation. The lattice can only accurately accommodate embeddings where the radius of curvature, $1/C$, is locally much greater than the spacing between lattice points. We have no hope of maintaining accuracy at a vertex, which is a near singularity, but we try to stay within an operating range where the sharpest features away from vertices have radii of curvature at least a few times the interlattice point spacing. This indirectly constrains the thickness of the elastic manifold we simulate, since features become sharper as the manifold is made thinner.

Our standard simulational procedure was to begin with a lattice about 30 units on a side, since this was the smallest lattice where fine features were clearly visible. After the elastic energy of the manifold was minimized on this lattice, we interpolated the result onto an 80-unit lattice and minimized again. Then we decreased the elastic thickness of the manifold on the larger lattice over a process of several minimizations. When the elastic thickness of the manifold becomes very small, the material becomes prone to falling into broad local minima with fine-scale crumpling that confuses the energy data. Slowly decreasing the thickness is a method to avoid this fine-scale crumpling. In most of the following sections we present the result of simulations on 80-unit lattices with an elastic thickness of ≈ 0.02 lattice units. The entire process of generating each minimized lattice took up to several weeks on a 233 MHz, Pentium-II based linux computer using a gcc compiler.

We note that our lattice simulates a phantom *m*-sheet, which can pass through itself without penalty. Since the energetic properties we study follow from local laws, and we stay in a thickness regime where curvature is nonsingular almost everywhere, the fact that our sheets are not self-avoiding does not affect the conclusions we draw from our data. The effect of the phantom *m*-sheet behavior on the dimensionality of vertex structures, where curvature does become singular, is discussed in Sec. X. In particular, as the thickness goes to zero, the minimum energy configurations need not converge to objects that have the local structure of a manifold. For example, in the vicinity of a vertex in a

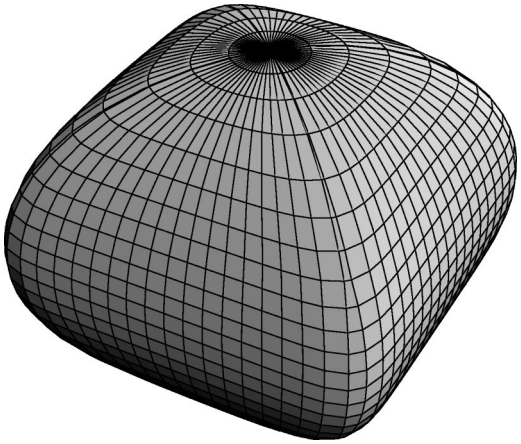

FIG. 4. Equipotential surface of the spatially confining potential for a square two-sheet embedded in three dimensions.

phantom sheet, as $h \to 0$, the configuration might converge to a branched manifold (e.g., a cone that winds twice around some axis).

For geometries that generated several disclinations in a single manifold, we took special care with initial conditions to insure that the system moved towards a symmetric final state. Relaxed states that contained a collection of identical vertices gave much cleaner scaling and always had a lower total energy than those that contained an ensemble of vertices with different local structure. Thus, when we started the sheet in a state with several folds, we separated the opposite sides of the folds slightly in globally symmetric ways to determine how they would relax.

VI. SPATIALLY CONFINED SHEETS

In this and the next three sections we report the results of our simulations. In this section we explore the distortions resulting from spatially confining our three-sheet in a contracting volume. Spatial confinement was simulated with an $(R/b)^{10}$ potential, which acts essentially like a hard wall at a radius b. We tailored the potential to our cube-shaped three-sheet by making the equipotential lines nearly cubical in three spatial dimensions and spherically symmetric in all remaining dimensions. This reduced edge effects at the corners of our cubes. The exact form of the potential was

$$E \propto \sum_{i=1}^{3} \left[\left(\frac{x_i}{b} \right)^2 + \sum_{j=4}^{d} \left(\frac{x_j}{b} \right)^2 \right]^5 . \tag{19}$$

An equipotential surface of this potential for a two-sheet in $d=3$ is shown in Fig. 4.

We began our simulations with the hard wall potential just outside the boundaries of the cube, then progressively moved the walls inward on all sides until the geometrically confining volume had only half the spatial extent of the resting cube in any direction. The value of b was decreased in ten equal steps, with the lattice allowed to relax to an elastic energy minimum after each step. This procedure simulates a gentle confinement process, which allows applied stress to propagate through the entire manifold volume instead of being caught in a strong ridge network at the outside edges. Gentle confinement is essential to good convergence of the inverse gradient routines used to minimize the elastic energy.

Since the spatial confinement technique requires multiple inverse gradient minimizations for each simulation, it is not computationally practical to run on large grids. Also, the data obtained from this method do not lend itself as well to numerical analysis, since the energy gradient from the tails of the hard wall potential mix with the elastic energy densities. Still, simulations performed on smaller grids (20 lattice units extent) show some interesting qualitative differences between confinement in $d=4$ vs $d=5$. As Fig. 5 shows, the regions of highest energy density are well organized line-networks for $d=4$ but are much more scattered and disorganized for $d=5$. Our arguments for the minimal dimensionality of $\mathcal{D}$ presented in Sec. III A predict a minimal dimension of 1 and 0 respectively for three-sheets embedded in four and five dimensions. If we assume that the high-

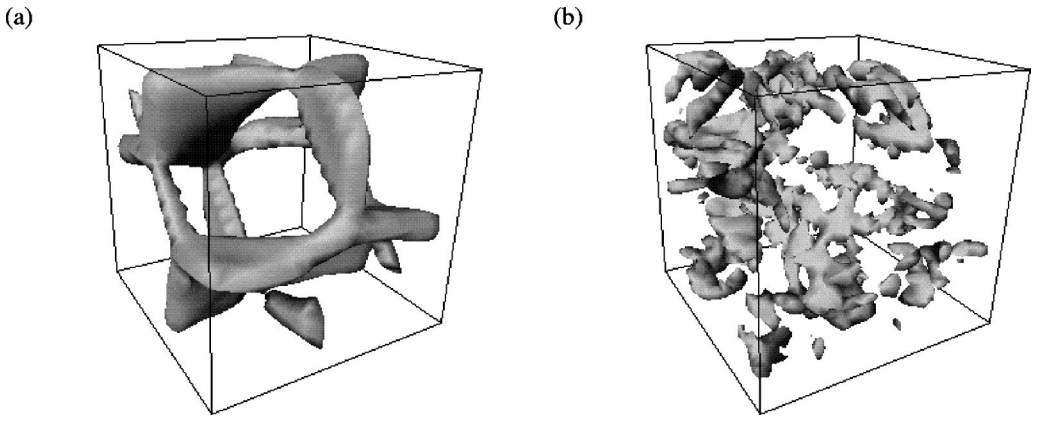

FIG. 5. Energy condensation map for spatially confined cubes. The cubes were $X=20$ lattice sites wide and had elastic thickness $h=0.075X$. Image (a) shows a surface of constant bending energy density in the material coordinate system for a cube embedded in four dimensions. The surface encloses the $\approx 10\%$ volume fraction with the highest energy concentration. Image (b) shows a surface of constant bending energy density for a cube embedded in five dimensions. This surface encloses the $\approx 7\%$ volume fraction. The wireframes represent the edges of the cubes' material coordinates.

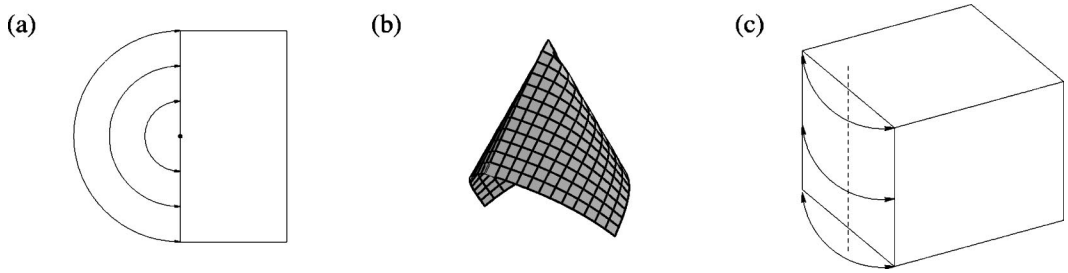

FIG. 6. Method for creating disclinations. In (a), one edge of two-sheet is folded and attached as shown. Points on the edge are identified, but the curvature is not continued across the seam. Image (b) shows an equilibrium configuration of a two-sheet constructed as in (a) after elastic energy minimization (as in Fig 3). Illustration (c) shows how the same technique is used to make a line disclination in a cubic three-sheet.

energy regions seen in Fig. 5 surround parts of $\mathcal{D}$, then the qualitative data supports these values for $\dim \mathcal{D}$.

VII. DISCLINATION PAIRS

To gain a better understanding of elastic energy condensation in *m*-sheets, we analyze several simpler forms of distortion. We first study pairs of disclinations. One way to create a disclination in a square two-sheet is to join two adjacent corners and the edge connecting them, as shown in Fig. 6(a). The disclination relaxes into a conical shape like that shown in Fig. 6(b). Placing two or more conical disclinations in a two-sheet in $d=3$ causes formation of ridges that are apparently equivalent to those connecting vertex singularities in a confined sheet. A corresponding technique for creating folds in a three-sheet is to add linelike wedge disclinations into the manifold. We simulate line disclinations in three-cubes numerically by folding faces of an elastic cube down the center and connecting the two halves as shown in Fig. 6(c).

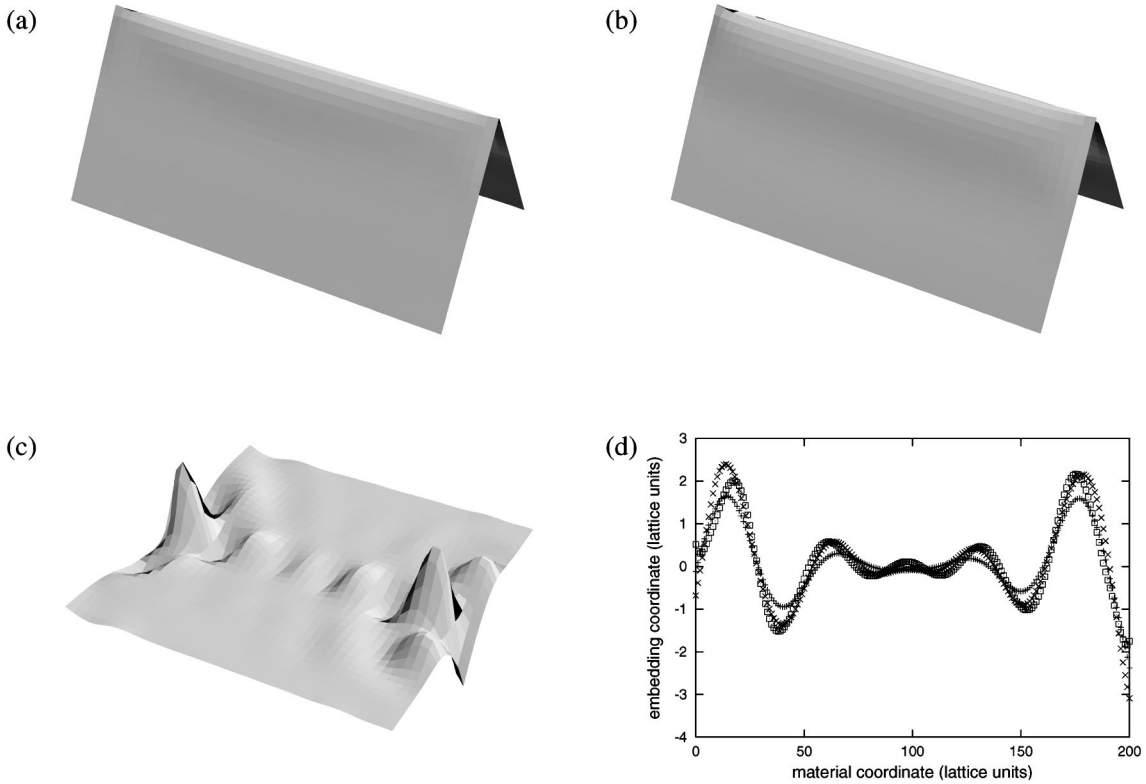

FIG. 7. Equilibrium embedding coordinates for elastic two-sheets with two 90° bends. The sheets were $X=200$ lattice sites wide and had elastic thickness $h=2\times10^{-4}X$. The bends were imposed by attaching opposite edges to a rigid right-angle frame. Image (a) shows the three embedding coordinates for a two-sheet in three-dimensional space. Image (b) shows the same three embedding coordinates for a two-sheet in four-dimensional space. Image (c) shows the fourth embedding coordinate [not shown in (b)] for the two-sheet in four-dimensions, plotted against the sheet's material coordinates. In (c), the value of the embedding coordinate has been multiplied by 20 to enhance contrast. In (d) the embedding coordinate shown in (c) is plotted against material coordinate down the folding line for three different material thicknesses. The (+) symbols correspond to an elastic thickness of 1 lattice unit, the (×) symbols correspond to an elastic thickness of 0.1 lattice unit, and the (□) symbols correspond to an elastic thickness of 0.01 lattice unit.

It can be shown by construction that the three-cube in embedding space $d>3$ can accommodate one line disclination without stretching. One can construct such an embedding by bending each plane perpendicular to the line disclination into an identical cone. However, pure bending configurations for a three-cube with two such line-disclinations will in general require folds. It is energetically favorable for the cube to stretch to avoid singular curvatures, so we may expect the sheet to form ridges with the same degree of elastic energy condensation as in a physically confined three-sheet.

We begin our study of disclinations in general dimensions by simulating a two-sheet with two sharp bends embedded in either three or four-dimensional space. From previous work [23] the two-sheet in three dimensions should form a simple ridge—its expected behavior in four dimensions is not known. Next we turn our attention to three-sheets, beginning with a simulation of a half-cube with a single line disclination embedded in either four or five dimensions. This simulation will verify the predicted scaling of a simple cone. Then, to induce elastic energy condensation we construct three-cubes with two line disclinations at opposite cube faces and embed them in four or five dimensions. Since there is no guarantee that our procedure will find the global energy minimum, we start the cubes in many different initial conditions. We investigate the behaviors when the line disclinations are either parallel or perpendicular to one another in the material coordinates.

A. Two-sheet: Two sharp bends

The behavior of two-sheets with two disclinations in three-dimensional space has been studied extensively [22], and our simulations of this geometry reproduced familiar results. However, we found for a variety of material thicknesses and disclination geometries that the behavior of the same two-sheets embedded in four dimensions was remarkably different. The data presented here is for a sheet geometry that is closely related to imposed disclinations and displayed the sheet's behavior particularly well. Instead of creating a disclination like that in Fig. 6(a), we fold opposite edges of the sheet and attach them to rigid frames with sharp bends at their centers. Each frame keeps the edge straight with a 90° angle at its center point. The frames are free to translate or rotate in the embedding space. This boundary condition is close to the conditions used to create ''minimal'' ridges in Ref. [22]. In that work Lobkovsky argued that the configuration of the sheet around a bending point on the edge will be much like that around a vertex. We found that the quantitative behavior of this boundary condition was consistent with that of imposed disclinations, but it allowed for more flexibility. The equilibrium embeddings of sheets with this geometry are shown in Fig. 7. Figure 8 presents plots of energy density versus area for three and four dimensional embeddings, and Fig. 9 plots local bending and stretching energy densities in the sheets' coordinate systems.

It is immediately evident from Figs. 9 that the stretching energy density in the region between the two sharp bends is greatly diminished in the four-dimensional embedding compared to the three-dimensional embedding. For the latter embedding, the line of high stretching energy density in Fig. 9(b) marks the presence of the stretching ridge. However, there is no such stretching line in the four-dimensional embedding energy map plotted in Fig. 9(d), even though Fig. 7(b) shows that there is still a folding line between the sharp bends in four dimensions. The energy plot in Fig. 8(a), for three-dimensional embedding, shows the parallel scaling of bending and stretching energies that is indicative of a ridge, but the energy plot in Fig. 8(b), for four dimensions, is more suggestive of conelike scaling, since the stretching energy falls twice as fast as bending energy away from the sharp bends.

Examining the embedding coordinates of the manifold in four dimensions, we found that the sheet mainly occupied

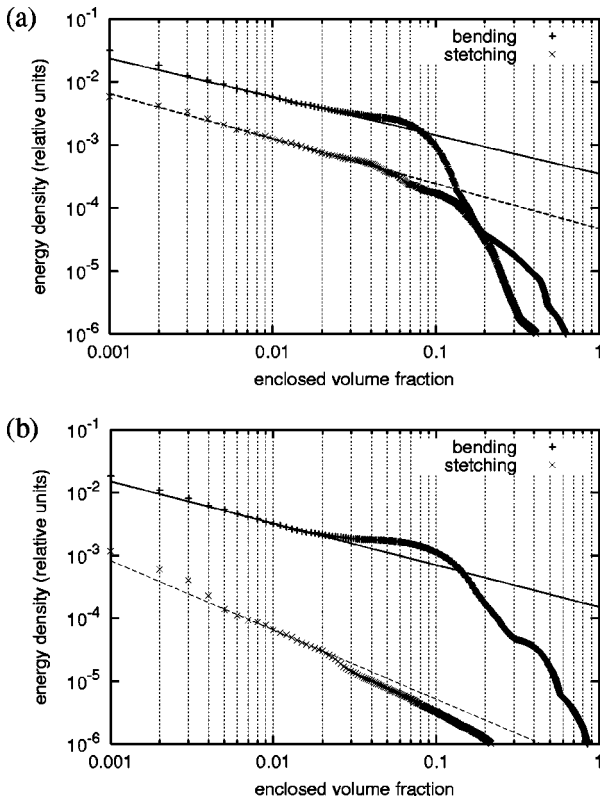

FIG. 8. Energy density plots for elastic two-sheets with two sharp bends. The sheets were $X=200$ lattice sites wide and had elastic thickness $h=2\times10^{-4}X$. In each graph the + symbols denote bending energy while the × symbols denote stretching energy. Energies are expressed in arbitrary units. Horizontal axes are area fraction Φ. Graph (a) shows local stretching energy density $\mathcal{L}_s$ and bending energy density $\mathcal{L}_b$ vs area fraction Φ at or above this energy density from an embedding in three dimensions. Graph (b) shows the same quantities from an embedding in four dimensions. In both graphs the straight lines are power law fits to the bending and stretching energy densities. In all graphs the energy fits are to the region between 0.5% and 2.0% volume fraction. In (a), the solid line is a fit to the bending energy density, with scaling exponent -0.61, and the dashed line is a fit to the stretching energy density, with scaling exponent -0.71. In (b), the solid line is a fit to the bending energy density, with scaling exponent -0.66, and the dashed line is a fit to the stretching energy density, with scaling exponent -1.10.

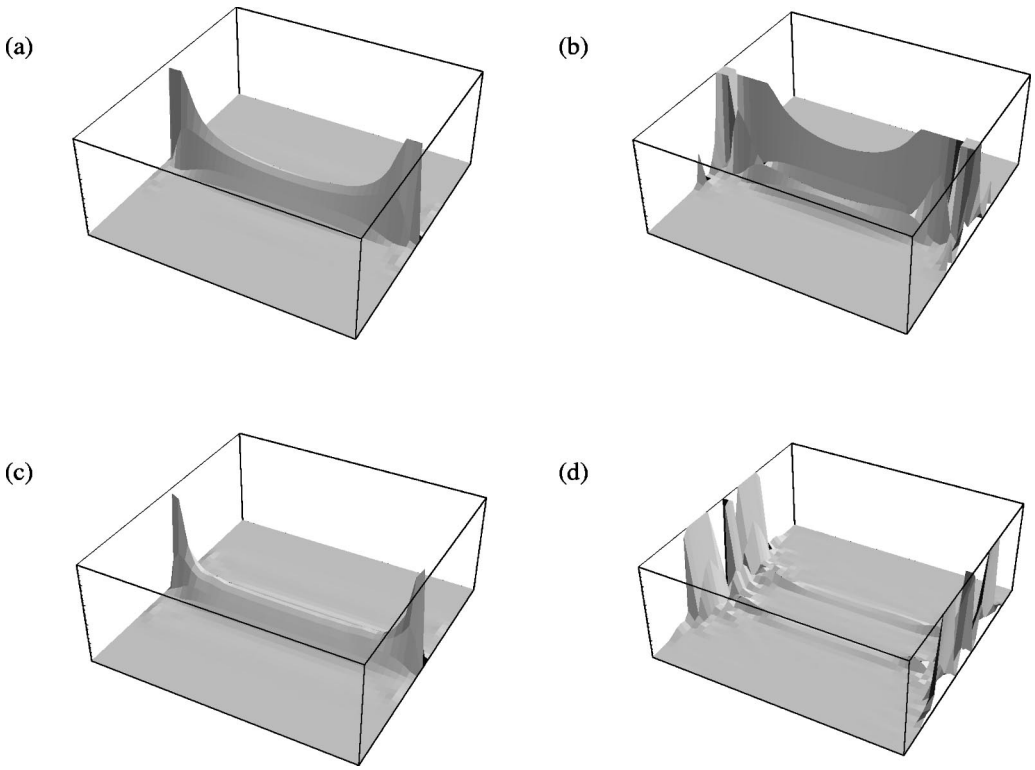

FIG. 9. Elastic energy density profiles in two-sheet with two sharp bends pictured in Fig. 7. The sheets were $X=200$ lattice sites wide. The elastic thickness of each was $h=2\times10^{-4}X$. In each plot the height of the surface is proportional to energy density in relative units and the x and y coordinates are the material coordinates in the manifold. The same energy units are used in all four plots. Plots (a) and (b) are for a three-dimensional embedding, plots (c) and (d) are from a sheet embedded in four dimensions. Plots (a) and (c) are the bending energies in the two-sheets, plots (b) and (d) are the stretching energies.

only three of the four available spatial dimensions. Figure 7(c) plots the value of the embedding coordinate with the lowest moment of inertia (the moment for the entire manifold in this direction is four orders less than that in other directions, in a frame where the inertia tensor is diagonal). We believe this slight bubbling into the extra dimension acts as a sink for compressive stress along the line connecting the sharp bends. Since this deviation is so small, one of the two normals to the manifold lies mostly in this direction over the entire surface. The curvature shown in Fig. 7(c) is small compared to the major component of curvature across the folding line, and is nearly orthogonal to it, so it has little effect on the total bending energy. Yet, in the thin sheets we simulate, the resulting changes in the strain field affect the stretching energy enormously.

The bubbling discussed above is evidence of an interaction between the sharp bends, since such a configuration is not seen for isolated disclinations or vertices and must be energetically less favorable than perfectly straight cone generators. If the sharp bends interact in a way that depends on the distance between them relative to the elastic thickness, then there might be some analog of a higher-dimensional ridge between them, with much weaker stretching energy. We did not see ridgelike parallel scaling in Fig. 8(b), but it is possible that the strain in this kind of ridge is so weak, and the virial ratio between bending and stretching is correspondingly so high, that the systems we simulated were dominated by a conelike configuration near the sharp bends and not by the ridge between them. If this is the case, our stretching energy graph shows only the initial energy falloff away from the sharp bends and never reaches the energy density value at which parallel scaling would commence. We can use the graph to put a lower limit on any possible virial relation by noting that conelike scaling continues to at least 2% volume fraction, at which point the ratio between bending and stretch energy densities is ≈ 70. Thus, if the bending and stretching energies do scale with elastic thickness, they should satisfy $E_b > 70E_s$.

Following the derivation presented in the Appendix, we can use the virial relation to put limits on the scaling exponents for the typical curvatures and strains on the ridge. For the above virial ratio, in the $h\rightarrow 0$ limit the typical midridge curvature would increase more slowly than $(X/h)^{1/35}$ and the typical ridge strain would fall faster than $(h/X)^{34/35}$, where h is the elastic thickness and X is the length of the folding line. To test our scaling hypothesis, we probed the deviation into the normal direction shown in Fig. 7(c). We estimate that the inverse square of the height of these bumps is proportional to the residual Gaussian curvature and therefore the strain along the ridge. In simulations of the same system at several different thicknesses, spanning two orders of magnitude, we could not discern a consistent change in the peak-to-peak height along this second normal [see Fig. 7(d)]. Since our ridge scaling arguments tell us we should see clear scaling of this peak-to-peak height with thickness, we conclude that

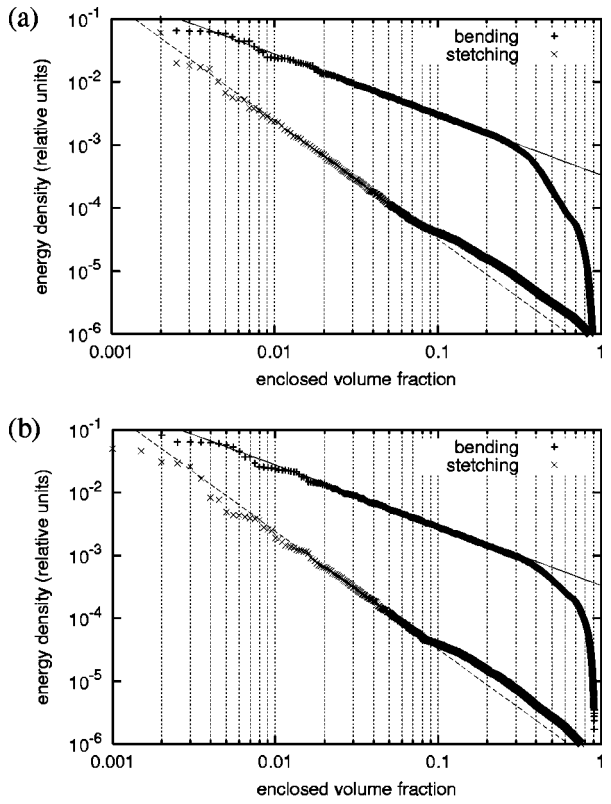

FIG. 10. Energy density plots for elastic half-cubes with single line disclinations. The rectangular solids were $X=40$ lattice sites across perpendicular to the face with the disclination and 80 sites wide in the other directions. They had elastic thickness $h=2.5\times10^{-4}X$. In each graph the $+$ symbols denote bending energy while the $\times$ symbols denote stretching energy. Energies are expressed in arbitrary units. Horizontal axes are volume fraction Φ. Graph (a) shows local stretching energy density $\mathcal{L}_s$ and bending energy density $\mathcal{L}_b$ vs volume fraction Φ at or above this energy density from an embedding in four dimensions. Graph (b) shows the same quantities from an embedding in five dimensions. In both graphs the straight lines are power law fits to the bending and stretching energy densities in the region between 2.0% and 10% volume fraction. In (a), the solid line is a fit to the bending energy density, with scaling exponent -0.95, and the dashed line is a fit to the stretching energy density, with scaling exponent -1.87. In (b), the solid line is a fit to the bending energy density, with scaling exponent -0.95, and the dashed line is a fit to the stretching energy density, with scaling exponent -1.87.

either we are not close enough to the thin limit for any potential scaling behavior to be evident, or the equilibrium configuration is really a higher-dimensional variation of simple cone scaling, which is truly independent of elastic thickness and fold length. These tests were run at (h/X) ratios from 10^{-3} to 10^{-5}, the entire range of thicknesses our simulations can handle and a region where two-sheets in three dimensions show very clear thickness scaling. It is clearly beyond our computational capabilities to resolve this potential scaling behavior.

B. Three-sheet: Single disclination

To verify our numerical predictions for the cone, we simulate an elastic half-cube with a single line disclination on one face. We use a $40\times80\times80$ unit lattice. The minimum energy embedding is a virtually identical cone in all the planes perpendicular to the line disclination. The radius of the cone ranges from 40 to $\sqrt{2}\times40$ lattice units. Figure 10 show the scaling of bending and stretching energy densities away from the disclination for both four and five-dimensional embeddings. In both cases the scaling exponents are very close to the theoretical values of -1 for bending and -2 for stretching for a cone with two-dimensional symmetry. We are quite satisfied that the elastic lattice can accurately represent the cone around a single disclination.

C. Three-sheet: Parallel disclinations

Apart from boundary conditions, the cube with parallel disclinations has a natural symmetry along the direction of the disclinations. We found that for all initial conditions tested, energy minimization resulted in a final configuration that showed this same symmetry (see Fig. 11). The manifold has no strain or curvature in the direction parallel to the disclinations, and very similar configurations for all planes perpendicular to this direction. In principle, for embedding in d dimensions, the configuration in each of the perpendicular planes is identical to that which we would expect for an elastic two-sheet with the same thickness to length ratio embedded in $d-1$ dimensions. In practice, we find that the extra material dimension adds an additional stiffness against fine scale crumpling that often confuses similar simulations in two-sheets.

For four-dimensional embedding the equilibrium configuration is a ''stack of ridges,'' which shows the same energy scaling as a ridge in three dimensions. Figure 12(a) is a plot of energy density vs volume for a three-cube with parallel disclinations in four dimensions. Within the high energy region encompassing $\approx2-8\,\%$ volume fraction, the ratio of bending energy density to stretching energy density at a given volume fraction is ≈6.2. This number is consistent with the theoretical energy ratio of 5. In this volume range the plots also confirm the lack of condensation *along* the ridge of both bending and stretching energies as well as the identical scaling of these energies. For the entire region up to $\approx30\%$ volume fraction the bending and stretching energy have roughly the same dependence on volume, though they do not fit a clean scaling exponent for any extended region. The sharp dropoff of the dominant energy above 30% volume fraction shows the significant condensation of energy around the ridge structure.

In contrast to the ridge-scaling in four dimensions, the energy scaling behavior of the sheet embedded in five dimensions appears conelike. The stretching scaling exponent of -1.59 indicates that the stretching energy is condensed at the vertices, while the bending exponent of -0.93 is consistent with -1, the predicted bending scaling of isolated line disclinations. The scaling data, as well as the lack of a strong ridge region in Fig. 11(b), indicate that the scaling around each disclination is not strongly influenced by interaction between the two disclinations. The scaling resembles that around the isolated disclination reported in Sec. VII B.

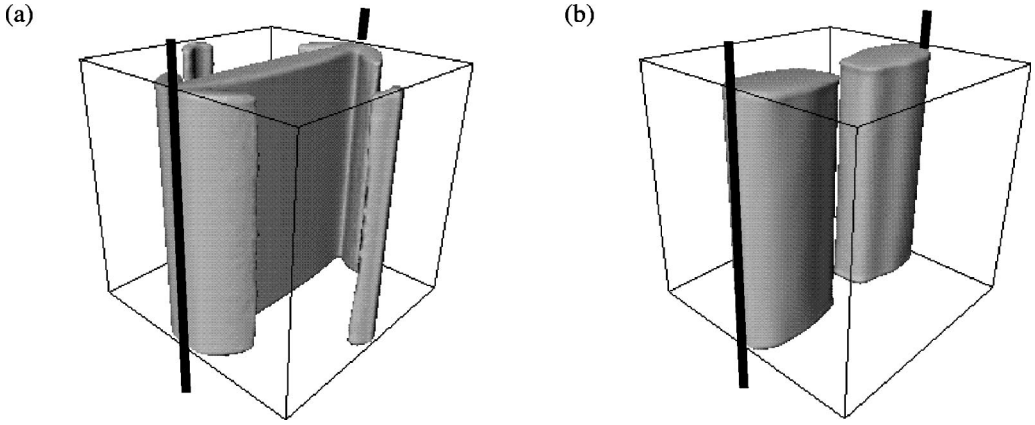

FIG. 11. Energy condensation map for cubes with parallel disclinations. The cubes were $X=80$ lattice sites wide and had elastic thickness $h=2\times10^{-4}X$. Image (a) shows a surface of constant bending energy density in the material coordinate system for a cube embedded in four dimensions. The surface encloses $\approx10.0\%$ volume fraction and shows energy condensation along the ridge which spans the gap between the disclinations. Image (b) shows the same surface for a cube embedded in five dimensions. The wireframes represents the edges of the cubes' material coordinates. Heavy lines mark the locations of disclinations.

D. Three-sheet: Perpendicular disclinations

A typical spatial energy distribution after energy minimization for a cube with perpendicular disclinations embedded in $d=4$ is shown in Fig. 13(a). A common feature of all the cubes embedded in four dimensions is the spontaneous appearance of additional linelike vertex structures. Spanning the volume between vertices and disclinations are two-dimensional ridges. This result is consistent with the $d=4$ geometrical confinement simulations detailed in Ref. [34]. Figure 14(a) shows the decay of local energy density with volume away from ridges and vertices for an elastic cube with nonparallel disclinations in four dimensions. The highest-energy regions correspond to the imposed disclinations and spontaneous vertex network. Lower energy regions correspond to ridges. The region between 1% and $\approx5\%$ volume fraction shows smooth scaling of bending and stretching energy densities with volume in a region dominated by the high-energy part of ridge structures (where they join at vertices). In this region the bending energy density scales with exponent -0.77 and the stretching with exponent -0.91. The values of the scaling exponents in this region are reasonably close to each other and to the theoretical scaling of $-4/5$ derived in Sec. IV. The scaling is clearly distinct from that of a cone, where the stretching energy density is expected to fall faster than Φ^{-1}.

The behavior of the same cubes placed in $d=5$ was quite different [see Fig. 13(b)]. For this embedding there is no spontaneous ridge-vertex network between the imposed disclinations. The difference in structure is reflected in the energy density plot, Fig. 14(b). In the volume fraction that typically encompasses high-energy structures apart from vertices and disclinations, the bending energy scales with volume with an exponent of -0.90 while the stretching energy scales with an exponent of -1.65. These numbers indicate the dominance of conical scaling near the vertices. They are similar to the scaling exponents for the cube with parallel disclinations in five dimensions. Figure 15 shows that the embedding appears to be locally conical around a disclination, without any evidence of folds. We surmise that the sheet has relaxed to a configuration where the cones around each line vertex interpenetrate without interacting strongly. This result demonstrates that in higher-dimensional crumpling, multiple vertices can exist in a sheet without requiring folds, for some geometries.

For this simulated geometry and several of the following, we present data for thicker sheets in four dimensions than in five. This is because the ridges found in four dimensions become very sharp as h gets smaller, and we typically present the thinnest data that do not show signs of finite lattice effects [like those seen below in Fig 17(a)]. For five-dimensional embeddings, decreasing the thickness typically shifts all the stretching energy densities upward and thereby extends the volume of cone scaling visible before the stretching energy density fades to background levels. We thus chose to present data from thinner sheets for five dimensions. We found that ridge scaling becomes more distinct as the sheet becomes thinner, so the use of thinner sheets in five dimensions only strengthens our claim that there is no evident ridge structure in five dimensions.

VIII. TOROIDAL CONNECTIVITY

Toroidal connectivity was simulated numerically by defining the lattice displacement vector, $\underline{\Delta}$, such that opposite faces of our cubic array had nearest-neighbor connections. The resulting connectivity was everywhere isotropic, with no borders or disclinations. Simulations were run for three-tori embedded in four, five, and six spatial dimensions. Initial conditions were either random or chosen to be very symmetric or close to possible energy minima. In all cases when $d=4$ or 5, minimization of the elastic energy resulted in energy condensation and the formation of high-energy networks. For six-dimensional embeddings the elastic energy was many times smaller than in lower dimensions and was uniformly distributed over the manifold. Figure 16 compares the energy condensation networks for three-tori embedded in

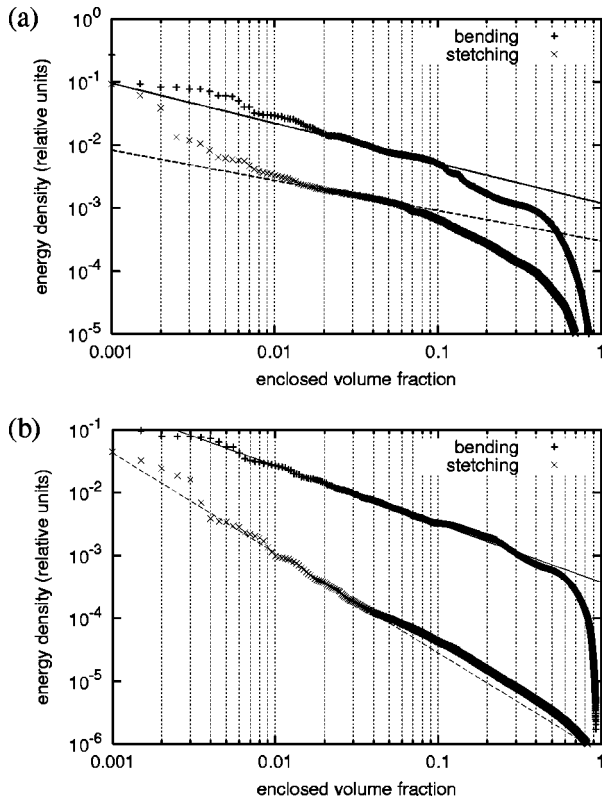

FIG. 12. Energy density plots for an elastic cube with parallel disclinations The cubes were $X=80$ lattice sites wide and had elastic thickness $h=2\times10^{-4}X$. In each graph the + symbols denote bending energy while the × symbols denote stretching energy. Energies are expressed in arbitrary units. Horizontal axes are volume fraction Φ. Graph (a) shows local stretching energy density $\mathcal{L}_s$ and bending energy density $\mathcal{L}_b$ vs volume fraction Φ at or above this energy density from an embedding in four dimensions. Graph (b) shows the same quantities from an embedding in five dimensions. In both graphs the straight lines are power law fits to the bending and stretching energy densities. In graph (a) the bending energy fit is to the region between 3.0% and 8.0% volume fraction and the stretching energy fit is to the region between 2.0% and 5.0% volume fraction. In graph (b) the fits are to the region between 1.0% and 4.0% volume fraction. In (a), the solid line is a fit to the bending energy density, with scaling exponent -0.63, and the dashed line is a fit to the stretching energy density, with scaling exponent -0.48. In (b), the solid line is a fit to the bending energy density, with scaling exponent -0.93, and the dashed line is a fit to the stretching energy density, with scaling exponent -1.59.

either four or five dimensions. Although the network is more extensive for $d=4$, in either dimension high-energy structures have comparable energy densities. We simulated this geometry beginning from many different initial conditions and the resulting final configurations showed varying degrees of asymmetry between the vertices. The configuration presented in Fig. 16(a) showed the highest degree of symmetry of all our four-dimensional torus simulations—its total elastic energy was $\sim25\%$ less than that of configurations that broke symmetry, so we believe it is most likely the true ground state of the system. Our energetic analysis was performed on this configuration.

The analog of ridges in the three-torus in $d=4$ are again planes of high elastic energy. These ridge structures meet in vertex-lines of very high elastic energy. Figure 17(a) shows the decay of local energy density with volume away from ridges and vertices for a three-torus in four dimensions. We fit a power law to the region that we identify as parts of ridges near the vertex structures. In this region the energy densities scale with an exponent of -0.87 for bending energy and -0.88 for stretching. These values are consistent with the theoretical ridge scaling exponent of $-4/5$ derived in Sec. IV. Within the ridge scaling volume the ratio of bending energy density to stretching energy density is 8.5, within a factor of 2 of the known value, 5, for two-sheets in three-dimensional crumpling.

The energy structures of tori embedded in $d=5$ were qualitatively different from those embedded in $d=4$ (refer again to Fig. 17). For $d=5$, the structures corresponding to vertices appear pointlike instead of linelike. The majority of the total energy density is concentrated around these pointlike vertices. Between vertices we were able to see smaller, linelike energy concentrations of elastic energy that could correspond to ridge structures. However, these regions occupied a miniscule volume in the manifold. The predominant energy structures were more symmetric and were centered around vertices.

Energy density vs volume is plotted in Fig 17(b) for an 80 lattice unit three-torus embedded in $d=5$. Smooth energy scaling begins at about 0.5% volume fraction and holds for up to $\approx10\%$ of the total volume. Within these high-energy regions the bending energy density scales with volume with an exponent of -0.56, whereas stretching energy density dies off more quickly, with a scaling exponent of -1.02. This is consistent with our simulations of line disclinations in five dimensions, since the stretching energy falls off nearly twice as fast as the bending energy. The number of vertices present in the manifold would lead us to expect ridges, but as we saw in Sec. VII C, ridges cannot be resolved by energy scaling alone in five dimensions at elastic thicknesses accessible to our simulations. The scaling exponents above are closer to the expected exponents of $-2/3$ and $-4/3$ for conical scaling around a pointlike disclination than to any other kind of scaling behavior we know. The embedding is probably close to this form of cone near the vertices.

IX. SINGLE FOLD (BOW CONFIGURATION)

In our final set of simulations we set our boundary and initial conditions to create single, pointlike vertices. Our aim was to verify scaling predictions for vertex deformations in four and five dimensions and to show clearly the existence of pointlike vertex structures in five-dimensional embeddings. According to the relations presented in Sec. II, a vertex is expected to have high Gaussian curvature. In more specific terms this means a vertex is a locus of strong curvature in at least two material directions along the same normal vector. Therefore, to force the existence of exactly one vertex in five dimensions (where every manifold point has two independent normals) we searched for a minimal set of boundary conditions that necessitated that some points in the manifold

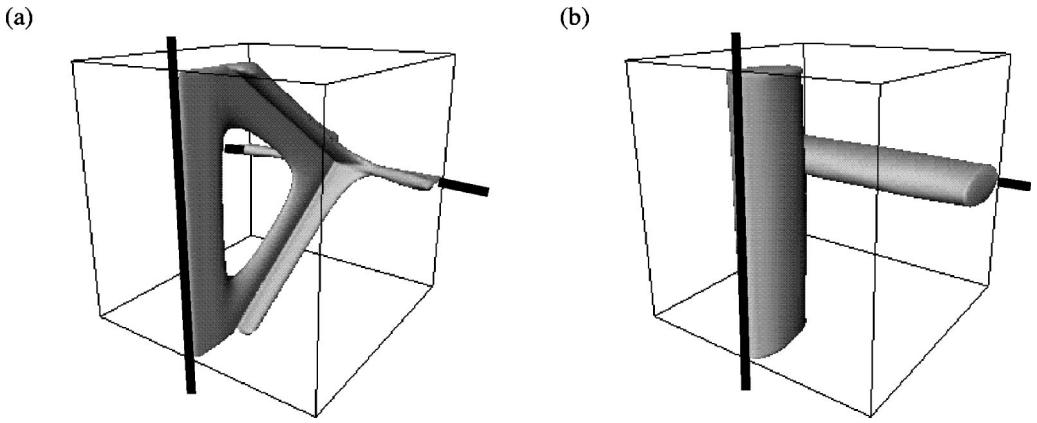

FIG. 13. Energy condensation map for cubes with perpendicular disclinations. The cubes were $X=60$ lattice sites across, 90 lattice units wide in the directions parallel to the disclinations, and had elastic thicknesses $h=6\times10^{-4}X$ (a) and $h=3\times10^{-4}X$ (b). Image (a) shows a surface of constant bending energy density in the material coordinate system for a cube embedded in four dimensions. Image (b) shows a surface of constant bending energy density for a cube embedded in five dimensions. The energy density value encloses $\approx3\%$ volume fraction in image (a) and shows the spontaneous vertex lines that arise between disclinations. In image (b) the equal energy density surface encloses $\approx10\%$ volume fraction and shows the growth of the high-energy region around the disclinations without additional vertices evident between them. The wireframes represent the edges of the cubes' material coordinates. Heavy lines mark the locations of disclinations.

have curvature in all three material directions. Our most successful simulations, presented here for four and five-dimensional embeddings of a three-cube, had only the center points of opposite faces attached. This geometry caused vertices to form while leaving the majority of the boundary free.

Figure 18 shows the pattern of energy condensation in three-cubes with attached opposite faces after energy minimization. For four-dimensional embeddings the surfaces of constant energy density enclose linelike regions that traverse the cube as seen in Figs. 18(a) and (b). The high-energy regions appear linelike all the way up to the highest values of the energy density. In contrast, the surfaces of constant energy density for five-dimensional embeddings form a series of shells, as seen in Figs. 18(c) and (d), whose typical diameters increase with decreasing energy density value. The energy density at the surface in Fig. 18(c), which encloses 0.1% volume fraction, is nearly an order of magnitude greater than the energy density at the surface of Fig. 18(d), which encloses 1% volume fraction and just touches the outside edges of the cube. These data clearly support our assertion that pointlike vertex structures are possible in five-dimensional embeddings. At the same time, they are consistent with conjectures [22] that the high-energy regions in four-dimensional embeddings are linelike. It may be noted that the five-dimensional embedding is asymmetric, while the four-dimensional embedding has a high degree of symmetry. We found that the elastic manifolds always spontaneously broke symmetry in five dimensions, but the minimum energy configuration we could find in four dimensions was perfectly symmetrical.

Plots of energy density vs enclosed volume fraction for this geometry are presented in Fig. 19. For four-dimensional embeddings the bending energy density does not scale with a simple exponent in the volume range between 1% and 10% volume fraction that we associate with the high-energy region of ridges. To get a representative value of the energy dropoff we fit a power law to the region between 3% and 10% volume fraction and find an exponent of -1.02. The stretching energy scales more cleanly in the region between 2% and 9% volume fraction, with an exponent of -0.75. The stretching energy exponent is close to the expected value of $-4/5$ and is smaller in magnitude than -1, so we can safely identify the scaling as ridgelike. When viewing the equal energy surfaces at larger volume fractions (not shown here) we saw a good deal of secondary structure in the ridges themselves, which could explain the many features in the energy density dependence.

For the five-dimensional embedding we fit a simple power law to the region of the graph that enclosed less than $\approx2\%$ volume fraction, since above this enclosed volume fraction the surfaces shown in Figs. 18(c) and (d) intersect the boundary of the cube [49]. In this region the bending energy density scales with an exponent of -0.65 while the stretching energy density scales with an exponent of -1.26. These numbers are consistent with the theoretical five-dimensional cone scaling exponent of $-2/3$ and $-4/3$ derived in Sec. IV.

X. DISCUSSION

In the numerical simulations reported in this paper, we have investigated the behavior of two and three-dimensional manifolds embedded in dimensions three and greater, subject to a variety of boundary conditions that cause crumpling. The results of our simulations, which are summarized in Table I, show a consistent dependence of the crumpling response on $d-m$, the difference between the dimensionality of the embedding space and that of the sheet. The behavior summarized in Table I can be described by the following general principles.

(1) For all the boundary conditions we consider, the dimensionality of spontaneous vertices $\mathcal{D}$ is $2d-m-1$, suggesting that the vertex dimensionality is always given by the *lower* bound from the arguments in Sec. III A that yield $\dim(\mathcal{D})\geqslant 2m-d-1$.

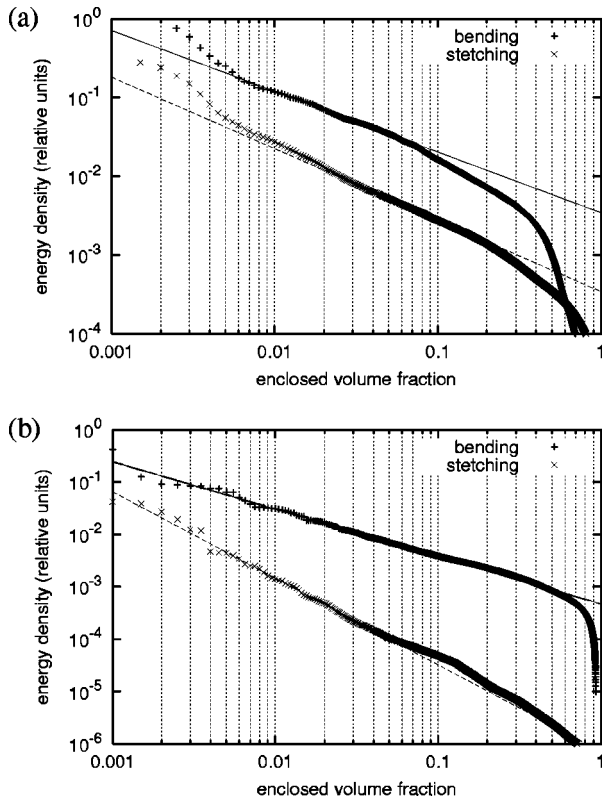

FIG. 14. Energy density plots for the elastic cubes with nonparallel disclinations in Fig 13. The cubes were $X=60$ lattice sites across, 90 lattice units wide in the directions parallel to the disclinations, and had elastic thicknesses $h=6\times10^{-4}X$ (a) and $h=3\times10^{-4}X$ (b). In each graph the + symbols denote bending energy while the × symbols denote stretching energy. Energies are expressed in arbitrary units. Horizontal axes are volume fraction Φ. Graph (a) shows local stretching energy density $\mathcal{L}_s$ and bending energy density $\mathcal{L}_b$ versus volume fraction Φ at or above this energy density from an embedding in four dimensions. Graph (b) shows the same quantities from an embedding in five dimensions. In (a), the solid line is a power law fit to the bending energy density in the region between 1.0% and 5.0% volume fraction, with scaling exponent -0.77, and the dashed line is a power law fit to the stretching energy density in the region between 3.0% and 10% volume fraction, with scaling exponent -0.91. In (b), the solid line is a power law fit to the bending energy density in the region between 1.0% and 10.0% volume fraction, with scaling exponent -0.90, and the dashed line is a power law fit to the stretching energy density in the region between 1.0% and 5% volume fraction, with scaling exponent -1.65.

(2) If $d=m+1$, the details of the curvature defect set $\mathcal{K}$ determine the nature of the energy condensation. For $\mathcal{D}=\mathcal{K}$ (no folding lines) we have the cone scaling discussed in Sec. IV, and for $\mathcal{K}-\mathcal{D}\neq\varnothing$ (folding lines present) we find ridge scaling.

(3) If $d\geqslant m+2$ we always find cone scaling if $\mathcal{K}\neq\varnothing$.

We believe that these principles are true in general. Consequently, they give explicit predictions for the behavior of elastic sheets in higher dimensions.

A. Effect of embedding dimension on defect dimension

Our data consistently supports the arguments presented in Sec. III A that for an m-dimensional manifold in d-dimensional space with $d<2m$, the dimensionality of the set $\mathcal{D}$ of vertex singularities will be greater than or equal to $2m-d-1$. In fact, we found that all spontaneous vertex structures had dimensionality $2m-d-1$ identically. For five-dimensional embeddings of three-sheets in which we did not explicitly make linelike disclinations, the manifolds were able to relax to configurations wherein $\mathcal{D}$ was small and pointlike. In contrast, when the embedding space was four dimensional for the same manifolds and boundary conditions, $\mathcal{D}$ was always linelike, terminating only at material boundaries. It is worth noting that in all cases where $\mathcal{D}$ was one dimensional, it was also piecewise flat—it is easy to argue that in order to minimize its spatial extent, $\mathcal{D}$ will in general be flat. Though our dimensionality arguments apply to only asymptotically thin sheets, the predictions appear well obeyed even for sheets as thick as 1/30 of their width. The dimensional behavior is thus much more robust than the ridge scaling behavior.

Because of the phantom nature of our simulated sheet, we found that favorable energy configurations often had local geometries at vertices in which the sheet passed through itself—the most common example was branched manifolds at vertices. The arguments for scaling and the minimum dimensionality of $\mathcal{D}$ are not affected by whether or not the sheets are phantom. However, the set of boundary conditions that produce nonphantom sheets with minimal vertex dimensionality may be more limited than for phantom m-sheets.

B. Effect of embedding dimension on scaling

In Sec. IV we made predictions for the energetic scaling outside of vertex structures for a sheet whose thickness was much smaller than its width. However, we did not analytically address how thin the sheet must be before it displays ''thin limit'' behavior. Our observations of the typical progress of a numerical simulation lend some insight into the approach to this asymptotic limit. In the process of relaxing our sheets, we often vary the thickness h, which shows us how the energy distribution depends on h. We were not able to vary h enough to directly observe any scaling behavior with h. Even our smallest h's show little enough of the desired asymptotic behavior, and increasing h only blurs this behavior beyond recognition. However, the qualitative behavior with h is consistent with our conclusions. The reported results are for the smallest h values we could reliably attain. When h is made larger, the main effect is to reduce the dynamic range in our energy density plots. It makes the energy spread more uniformly over the sheet. Where ridge scaling is observed, increasing h reduces the proportion of stretching energy, as we have previously observed in two-sheets [22]. Finally, increasing h reduces the observed effect of embedding dimension. The clear differences between the stretching and bending energy profiles in five dimensions become less distinct as h is increased. This is as expected. Embedding dimensions should have less effect if a sheet is

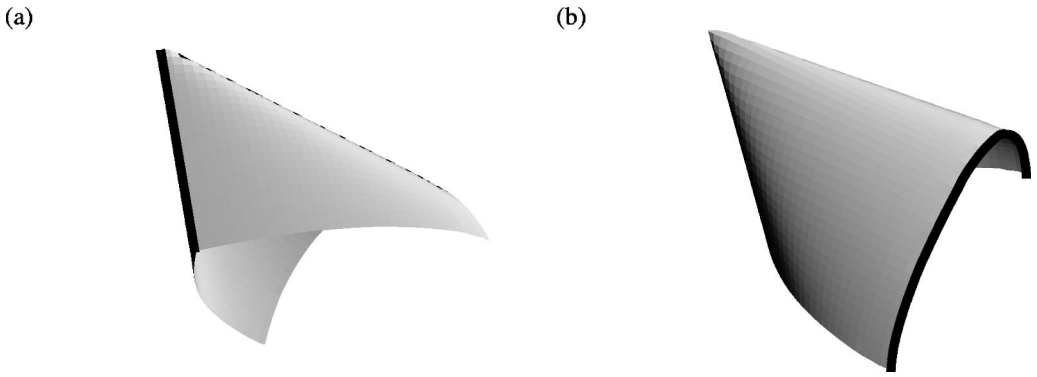

FIG. 15. Two views of a three-dimensional projection of the embedding coordinates for a two-slice from the material coordinates of a cube with nonparallel disclinations embedded in five dimensions. The material coordinate slice contains one disclination along the edge marked with the heavy line in (a). It is perpendicular to the other disclination, which is marked with a heavy line in (b). The views were chosen to show the conelike geometry about the disclination that the plane intersects at a point.

thicker. These behaviors add to our confidence that the scaling behavior we report becomes more, not less, distinct as we reduce h.

Our derivation of cone scaling was based on very simple and well-founded assumptions, so it was not a surprise that cone scaling was so clearly visible in geometries where we expected to find it. In all simulations where there was only one disclination structure in a three-dimensional manifold, the observed scaling was consistent with our predictions based on cones. A single line disclination in either four or five dimensions produced a cone structure with scaling like that of a simple cone in a two-sheet. In the simulations presented in Sec. IX, embeddings in five dimensions produced a pointlike vertex and energy scaling close to our predictions for double-cone scaling (where there is curvature on the same order in both material directions perpendicular to the cone generators). The success of these predictions assures us that the cone structure is well understood and that, for the case of line disclinations, the description of a relaxed configuration in terms of a stack of two-sheet embeddings can be accurate.

Our simulations verified the formation of ridges in two-sheets in three dimensions and in three-sheets in four dimensions, as witnessed in other studies [3,34]. As expected, planar ridge structures spanning the gaps between linear vertex structures in $d=4$ had the same energy-bearing properties as their three-dimensional equivalents. However, for two-sheets in four dimensions and three-sheets in five dimensions we consistently found no ridge energy structures, even along what appeared to be folds. In Fig. 7(c) it is apparent that the elastic sheet deflects slightly into the fourth dimension in order to relieve the strain along the ridge center. The way this ridge decreases the strain along its midline shows the essential difference between embeddings of m sheets in $m+1$ dimensions and in all greater dimensions. In the geometric von Karman equations, Eq. (9), the sources of strain are *sums* of curvatures along different normals. If there is more than one normal direction, then there is the possibility of cancellation

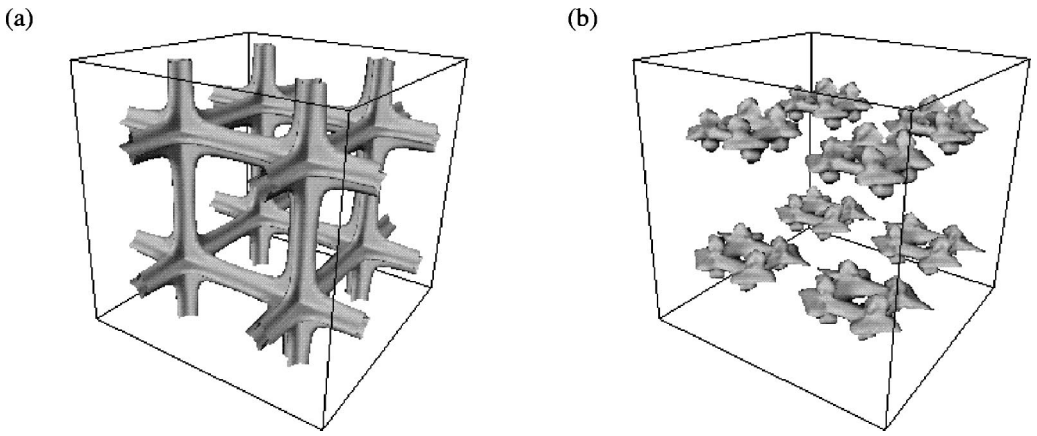

FIG. 16. Energy condensation maps for three-tori. The tori were made from cubes of width $X=80$ lattice sites and with elastic thicknesses $h=1\times10^{-3}X$ (a) and $h=2.5\times10^{-4}X$ (b). Image (a) shows a surface of constant bending energy density in the material coordinate system for a three-torus embedded in four dimensions. In this simulation the initial conditions were chosen to favor a symmetric relaxed state. Image (b) shows a surface of constant bending energy density for a three-torus embedded in five dimensions. The surfaces encloses $\approx2.5\%$ volume fraction in (a) and $\approx2.8\%$ volume fraction in (b). The wireframes represent the edges of the cubes' material coordinates.

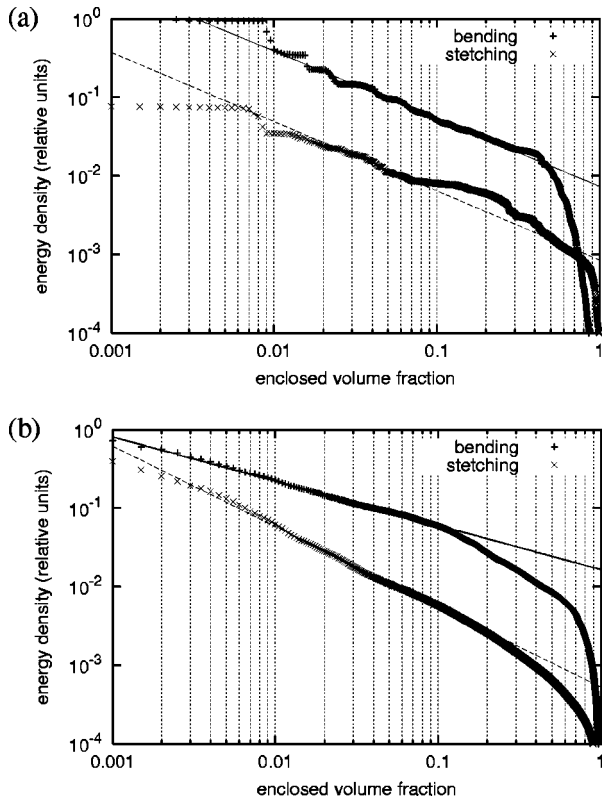

FIG. 17. Energy density plots for the three-tori in Fig. 16. The tori were made from cubes of width $X=80$ lattice sites and with elastic thicknesses $h=1\times10^{-3}X$ (a) and $h=2.5\times10^{-4}X$ (b). In each graph the + symbols denote bending energy while the × symbols denote stretching energy. Energies are expressed in arbitrary units. Horizontal axes are volume fraction Φ. Graph (a) shows local stretching energy density $\mathcal{L}_s$ and bending energy density $\mathcal{L}_b$ vs volume fraction Φ at or above this energy density from an embedding in four dimensions. The several plateaus in the high-energy part of the plot are an artifact of the discrete lattice. They reflect the nearly identical geometry of the points on and adjacent to the vertices, which make up a measureable fraction of the manifold volume. Graph (b) shows the same quantities as in (a) for an embedding in five dimensions. In (a), the solid line is a power law fit to the bending energy density in the region between 2.0% and 10% volume fraction, with scaling exponent -0.87, and the dashed line is a power law fit to the stretching energy density in the region between 2.0% and 6.0% volume fraction, with scaling exponent -0.88. In (b), the solid line is a power law fit to the bending energy density in the region between 0.5% and 10.0% volume fraction, with scaling exponent -0.56, and the dashed line is a power law fit to the stretching energy density in the region between 0.5% and 10% volume fraction, with scaling exponent -1.02.

between curvature terms for any given two-dimensional hyperplane. On the four-dimensional fold the manifold bubbles into the extra dimension, creating positive Gaussian curvature that counters the negative Gaussian curvature of the saddle-shaped peak-to-peak ridge profile (see, for example, Fig. 3). We do not assume that the cancellation of lowest-order terms is perfect, but we showed in Sec. VII A that the stretching energy is diminished so greatly relative to the bending energy that ridgelike scaling is completely masked by conical scaling near vertices (It is notable that, based on the scaling arguments derived in the Appendix, in the limit of very large virial ratios the dominant curvature terms become increasingly insensitive to the elastic thickness—much like they are in cones). We hope to return to this subject in future research, with the aim to find analytic expressions for the embedding of a two-sheet with two disclinations in four spatial dimensions and derive the thin limit scaling directly.

C. New questions raised by this work

We believe that the detailed structure of the novel point-like vertices in three-sheets deserves further study. For example, in Sec. IX we touched on the fact that these point vertices are loci of folding in all three material directions. Since the three material directions share only two normals and are constrained by the boundary conditions that the sheet be isometric outside the vertex point, it is likely that the angles each direction folds by can only take *discrete* sets of values—not unlike the discretization of disclination angles in a lattice, but driven purely by spatial geometry for an otherwise continuous medium. This discetization would probably be more pronounced in sheets that are not phantom, since branched manifolds at vertices add more degrees of freedom.

Much could also be learned by viewing these new crumpling phenomena as a mathematical boundary-layer problem, since they display several new and intriguing features in this light. Our problem belongs to the class of variational problems given by a singularly perturbed energy functional $\mathcal{E}^h$ with small parameter h. One approach to analyzing such variational problems is by identifying the boundary layers and then determining the appropriate solutions through matched asymptotics. Example of this ''local'' approach, as applied to elastic two-sheets are the analysis of ridges in Ref. [22] and of the vertices in Ref. [10].

A contrasting ''global'' approach to these problems is through the notion of Γ–convergence [44,45]. This approach calls for the identification of an appropriate asymptotic energy $\mathcal{E}^*$ that gives the energy of a configuration in the $h\rightarrow0$ limit. This asymptotic energy functional is called the Γ limit of the functional $\mathcal{E}^h$ as $h\rightarrow0$. If the Γ limit exists, the configuration of the minimizers for a small but nonzero h is then deduced by finding the minimizers for $\mathcal{E}^*$ and observing that the minimizer for nonzero h is close to the minimizer for $\mathcal{E}^*$. Note that this approach is similar in philosophy to our arguments in Sec. III where we deduced the structure of the vertex regions for $h>0$, by considering isometric immersions that are relevant for $h=0$.

Since these singularly perturbed variational problems show energy condensation, in the limit $h\rightarrow0$ all the energy concentrates on to a defect set, which we denote by $\mathcal{B}$. Consequently, the appropriate asymptotic energy should also be defined for singular configurations, and it should depend on the defect set $\mathcal{B}$, and the configuration u outside $\mathcal{B}$. Thus, the asymptotic energy is given by a functional $\mathcal{E}^*=\mathcal{E}^*[h,u,\mathcal{B}]$. Examples of this type of analysis are the analysis of phase separation in Refs. [18,19] and the asymptotic folding energy in the context of the blistering of thin films [25,26,29]. In both these cases, the asymptotic energy scales with the small

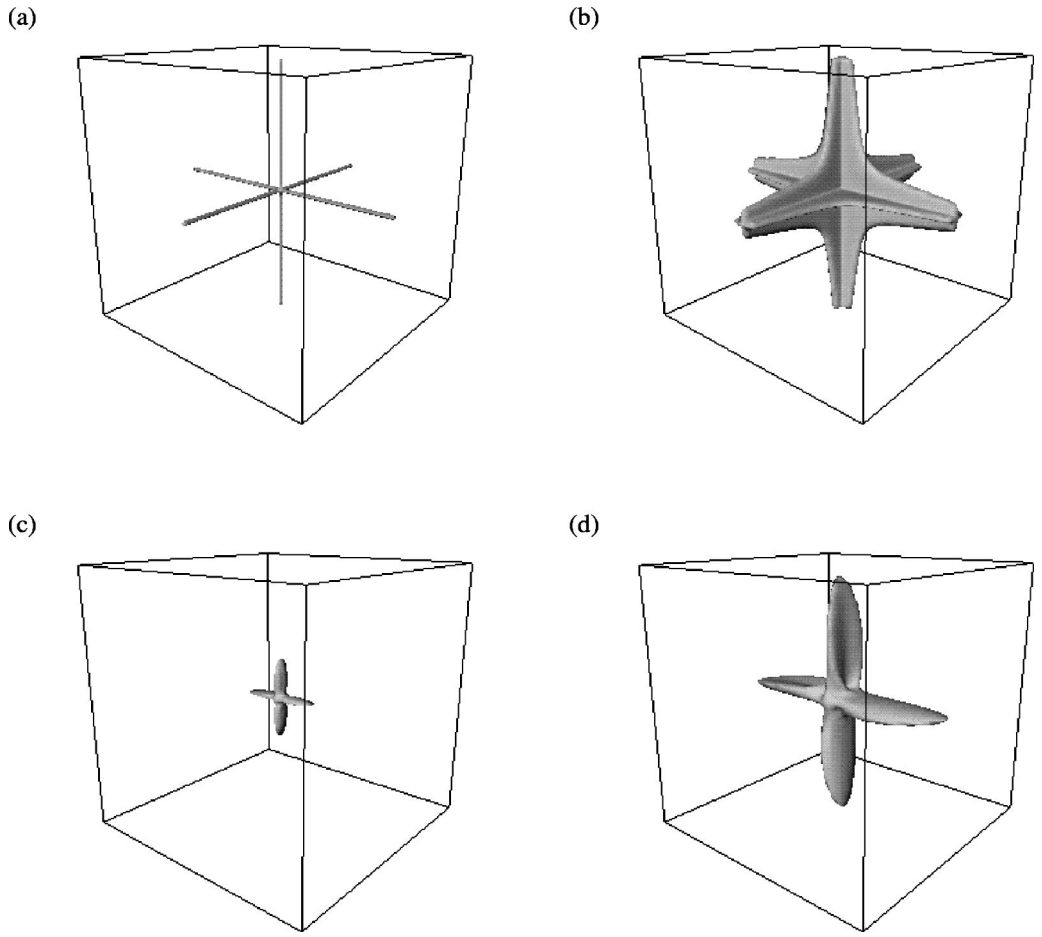

FIG. 18. Energy condensation maps for three-cubes with center points of opposite faces attached. The cubes were $X=80$ lattice sites wide and had elastic thickness $h=2.5\times10^{-4}X$. Images (a) and (b) show surfaces of constant bending energy density in the material coordinate system for a three-cube embedded in four dimensions. In this simulation the initial conditions were chosen to favor a symmetric relaxed state—many stable configurations show pronounced symmetry breaking in one direction. Images (c) and (d) show surfaces of constant bending energy density for a three-cube embedded in five dimensions. The surfaces in (a) and (c) enclose 0.1% volume fraction while those in (b) and (d) enclose 1%. The wireframes represent the edges of the cubes' material coordinates.

parameter h as $\mathcal{E}^*\sim h^\alpha$ for a fixed α. Also, the Γ limit is local, in that the asymptotic energy is given by integrating a local energy density over the defect set. This is in sharp contrast to the behavior of elastic manifolds. For elastic manifolds, the asymptotic energy depends on two kinds of defect sets, the strain defect set $\mathcal{D}$ and the curvature defect set $\mathcal{K}$. The exponent α that gives the scaling of $\mathcal{E}^*$ with h is not fixed, but depends on whether or not $\mathcal{D}=\mathcal{K}$. Finally, in the case of ridge scaling, we have the following two interesting features.

(1) The width of the boundary layer around the ridge depends on both the small parameter h and the length of the ridge X.

(2) The energy of the ridge scales as $h^{5/3}X^{1/3}$ and is not linear in the size of the ridge. Therefore, the asymptotic energy of the ridge is not given by an integral of a local energy density over $\mathcal{K}$.

These features imply that the Γ limit $\mathcal{E}^*$, if it exists, is nonlocal. It is, therefore, very interesting to carry out a rigorous analysis of the Γ limit for the elastic energy functional in Eq. (6). This analysis will probably involve new ideas and techniques.

Finally, current theories of matter and space-time suggest additional relevance for our findings. These theories [46] view the observed properties of matter and space as arising from the embedding of underlying manifolds into higher-dimensional spaces. Such postulates of higher-dimensional spaces giving rise to observed properties date back to Kaluza's [47] demonstration that electromagnetism can be viewed as a consequence of a fifth spatial dimension. Though our work has explored only the behavior of *elastic* sheets embedded in higher dimensions, many of our results concerning $\mathcal{D}$ and $\mathcal{K}$ are purely geometrical. Since the energetics of elasticity are relatively simple our geometric results may generalize to related theories, such as particle field theories. In the most general terms, we have demonstrated a circumstance in which manifold embeddings can give rise to interesting localized features with a dimesionality distinct from that of the manifold and the space [48].

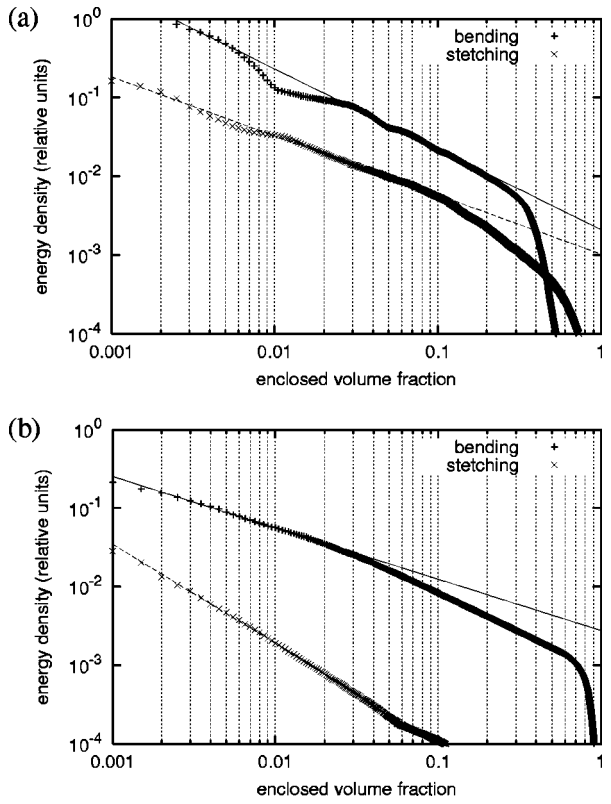

FIG. 19. Energy density plot for the elastic cubes with center points of opposite faces attached pictured in Fig. 18. The cubes were $X=80$ lattice sites wide and had elastic thickness $h=0.001X$. In each graph the $+$ symbols denote bending energy while the $\times$ symbols denote stretching energy. Energies are expressed in arbitrary units. Horizontal axes are volume fraction Φ. Graph (a) shows local stretching energy density $\mathcal{L}_s$ and bending energy density $\mathcal{L}_b$ vs volume fraction Φ at or above this energy density from an embedding in four dimensions. Graph (b) shows the same quantities from an embedding in five dimensions. In (a), the solid line is a power law fit to the bending energy density in the region between 3.0% and 10% volume fraction, with scaling exponent -1.02, and the dashed line is a power law fit to the stretching energy density in the region between 2.0% and 9.0% volume fraction, with scaling exponent -0.75. In (b), the solid line is a power law fit to the bending energy density in the region between 0.2% and 2.0% volume fraction, with scaling exponent -0.65, and the dashed line is a power law fit to the stretching energy density in the region between 0.2% and 2.0% volume fraction, with scaling exponent -1.26.

CONCLUSION

In this paper, we have found two important results for crumpled sheets. First, we have shown that if the spatial dimension d is greater than $m+1$, the stretching elastic energy condenses onto vertex structures, while for the special case $d=m+1$ it condenses onto ridges as well. Second, we have provided evidence that when $d<2m$ the strain defect set in a crumpled sheet has dimension at least $2m-d-1$. For higher-dimensional manifolds with $m>3$, one may imagine further forms of energy condensation as the embedding dimension increases. Such manifolds could reveal further surprises, as the present study did. Like gauge fields, elastic manifolds have revealed distinctive ways in which singularities in a field may interact at long range. To explore further the conditions and forms of this interaction seems worthwhile.

TABLE I. Summary of simulational results. The first three columns list the geometry of the simulated sheet and the spatial and embedding dimensions. The next column lists the dimension of any *spontaneous* vertex structures. The next column tells whether the observed scaling was conelike or ridgelike. The final column tells, for the cases where the boundary conditions did not explicitly break the three-dimensional symmetry of the cube, whether the energy minimum was a symmetric state in the manifold coordinates. The six manifold geometries, in the order presented here, are: two point disclinations in a square sheet, a single line disclination at one cube face, parallel line disclinations on opposite cube faces, perpendicular line disclinations on opposite cube faces, toroidal connectivity of a three-dimensional manifold, and the attachments of the center points of opposite cube faces to each other.

Geometry	m	d	Vertex Dimension	Scaling	Spontaneous asymmetry
Two sharp bends	2	3	n/a	ridge	n/a
	2	4	n/a	cone	n/a
Isolated disclinations	3	4	n/a	cone	n/a
	3	5	n/a	cone	n/a
$\parallel$ disclinations	3	4	n/a	ridge	n/a
	3	5	n/a	cone	n/a
$\perp$ disclinations	3	4	1	ridge	n/a
	3	5	n/a	cone	n/a
Torus	3	4	1	ridge	no
	3	5	0	cone	yes
Bow	3	4	1	ridge	no
	3	5	0	cone	yes

ACKNOWLEDGMENTS

The authors would like to thank Bob Geroch, L. Mahadevan, Bob Kohn, and Felix Otto for helpful and enlightening conversations. This work was supported in part by the National Science Foundation under Award number DMR-9975533 and by its MRSEC program under Award number DMR-9808595. S.C.V. was also supported by the Alfred P. Sloan Jr. Foundation.

APPENDIX: DERIVATION OF VIRIAL RELATION

Here we derive the relation between the energy scaling exponents and the virial ratio of bending to stretching energies on an elastic ridge. This derivation is a generalization of the derivation presented in Ref. [23].

We assume for simplicity that on a ridge, the elastic bending energy is dominated by the contribution of the main curvature accross the ridge, and this curvature is approximately constant for the entire length of the ridge with a typical value C. For a simple ridge of length X in a two-dimensional manifold, the ridge curvature is significant in a band of width $w=1/C$ transverse to the ridge, so the total bending energy of the ridge is approximately

$$\mathcal{E}_b \approx \mu h^2 C^2 w X = \mu h^2 C X, \tag{A1}$$

where μ is the elastic modulus of the material and h is the thickness.

If we assume that the ridge has a single dominant component of strain that also extends for a typical width w and has typical value γ, then the total stretching energy of the ridge is

$$\mathcal{E}_s \approx \mu \gamma^2 w X = \mu \gamma^2 X / C. \tag{A2}$$

We can write the total elastic energy along the ridge as

$$\mathcal{E} \approx \mu X [h^2 C + \gamma^2 C^{-1}]. \tag{A3}$$

Now, if we make a scaling ansatz, $\gamma \sim (XC)^{-\alpha}$, the energy becomes

$$\mathcal{E} \sim \mu X [h^2 C + X^{-2\alpha} C^{-(2\alpha+1)}]. \tag{A4}$$

We may now find the minimum energy balance by setting the derivative $d\mathcal{E}/dC$ equal to zero:

$$h^2 - (2\alpha+1) X^{-2\alpha} C^{-(2\alpha+2)} = 0 \tag{A5}$$

$$\Rightarrow C \sim X^{-1} (h/X)^{-1/(\alpha+1)} \tag{A6}$$

$$\Rightarrow \gamma \sim (h/X)^{\alpha/(\alpha+1)}. \tag{A7}$$

From the first of the above equations, it is clear that the virial ratio is related to α by $\mathcal{E}_b = (2\alpha+1)\mathcal{E}_s$.

[1] D.R. Nelson and L. Peliti, J. Phys. (France) **48**, 1085 (1987).
[2] H.S. Seung and D.R. Nelson, Phys. Rev. A **38**, 1005 (1988).
[3] A.E. Lobkovsky and T.A. Witten, Phys. Rev. E **55**, 1577 (1997).
[4] M. BenAmar and Y. Pomeau, Proc. R. Soc. London, Ser. A **453**, 729 (1997).
[5] M. BenAmar and Y. Pomeau, Philos. Mag. B **78**, 235 (1998).
[6] E. Cerda, S. Chaïeb, F. Melo, and L. Mahadevan, Nature (London) **401**, 46 (1999).
[7] A. Boudaoud, P. Patricio, Y. Couder, and M. Ben Amar, Nature (London) **407**, 718 (2000).
[8] L.A. Cuccia and R.B. Lennox, Abstr. Pap. - Am. Chem. Soc. **208**, 50 (1994).
[9] S. Chaïeb, F. Melo, and J.C. Geminard, Phys. Rev. Lett. **80**, 2354 (1998).
[10] E. Cerda and L. Mahadevan, Phys. Rev. Lett. **80**, 2358 (1998).
[11] S. Chaïeb and F. Melo, Phys. Rev. E **60**, 6091 (1999).
[12] J. Frohlich and U.M. Studer, Rev. Mod. Phys. **65**, 733 (1993).
[13] M. Nelkin, Science **255**, 566 (1992).
[14] L. deArcangelis *et al.*, Phys. Rev. B **40**, 877 (1989).
[15] M.F. Gyure and P.D. Beale, Phys. Rev. B **46**, 3736 (1992).
[16] A.M. Polyakov, Nucl. Phys. B (Proc. Suppl.) **68**, 1 (1998).
[17] S. Müller, in *Calculus of Variations and Geometric Evolution Problems*, edited by S. Hildebrandt and M. Struwe (Springer-Verlag, Berlin, 1999), p. 85.
[18] P. Sternberg, Arch. Ration. Mech. Anal. **101**, 109 (1988)
[19] R.V. Kohn and P. Sternberg, Proc. R. Soc. Edinburgh, Sect. A: Math. **111**, 69 (1989); I. Fonseca and L. Tartar, *ibid.* **111**, 89 (1989).
[20] F. Bethuel, H. Brézis, and F. Hélein, *Ginzburg-Landau Vortices* (Birkhäuser, Boston, 1994).
[21] K. Bhattacharya and R.D. James, J. Mech. Phys. Solids **47**, 531 (1999).
[22] A.E. Lobkovsky, Phys. Rev. E **53**, 3750 (1996).
[23] A. Lobkovsky, S. Gentes, H. Li, D. Morse, and T.A. Witten, Science **270**, 1482 (1995).
[24] M. Ortiz and G. Gioia, J. Mech. Phys. Solids **42**, 531 (1994).
[25] P. Aviles and Y. Giga, Proc. R. Soc. Edinburgh, Sect. A: Math. **129**, 1 (1999).
[26] W. Jin and R.V. Kohn, J. Nonlinear Sci. **10**, 355 (2000).
[27] B. Audoly, Phys. Rev. Lett. **83**, 4124 (1999).
[28] A. De Simone, R. V. Kohn, S. Müller, and F. Otto (unpublished).
[29] L. Ambrosio, C. De Lellis, and C. Mantegazza (unpublished).
[30] W. Jin and P. Sternberg (unpublished).
[31] W. Jin and P. Sternberg (unpublished).
[32] H.B. Belgacem, S. Conti, A. De Simone, and S. Müller (unpublished).
[33] E.M. Kramer, J. Math. Phys. **38**, 830 (1997).
[34] E.M. Kramer, T.A. Witten, Phys. Rev. Lett. **78**, 1303 (1997).
[35] S.C. Venkataramani, T.A. Witten, E.M. Kramer, and R.P. Geroch, J. Math. Phys. **41**, 5107 (2000).
[36] L.D. Landau and E.M. Lifshitz, *Theory of Elasticity* (Pergamon Press, New York, 1959).
[37] W.H. Press, S.A. Teukolsky, W.T. Vetterling, and B.P. Flannery, *Numerical Recipes in C* (Cambridge University Press, Cambridge, 1992).
[38] M. Spivak, *A Comprehensive Introduction to Differential Geometry* (Publish or Perish, Houston, 1979).
[39] T. von Karman, *The Collected Works of Theodore von Karman* (Butterworths Scientific Publications, London, 1956).
[40] G.B. Airy, Philos. Trans. R. Soc. London **153**, 49 (1863).
[41] R.M. Wald, *General Relativity* (The University of Chicago Press, Chicago, 1984).
[42] J.C. Maxwell, Trans. - R. Soc. Edinburgh **26**, (1870); reprinted in *The Scientific Papers of James Clark Maxwell* (Cambridge University Press, Cambridge, 1927), Vol. 2, p. 161.
[43] P. Patricio and W. Krauth, Int. J. Mod. Phys. C **8**, 427 (1997).
[44] E. DeGiorgi, Boll. Unione Mat. Ital. **14**, 213 (1977).
[45] G. Dal Maso, *An Introduction to* Γ*–Convergence* (Birkhäuser, Boston, 1993).
[46] E. Witten, Nucl. Phys. B **443**, 85 (1995).
[47] J.M. Overduin and P.S. Wesson, Phys. Rep. **283**, 303 (1997).
[48] By *subsheet* we mean a subset of the manifold lying in a subspace of $\mathbb{R}^m$.
[49] The broad region of the bending energy density graph between $\approx 2\%$ and $\approx 40\%$ volume fraction which seems to show clear scaling is well fit by a scaling exponent of ≈ -0.9. This suggests that the energy falls away slowly transverse to most energetic cone generators. This observation is not contradictory to our assumption that the region of high curvature persists for a length of order $1/C$ in the transverse directions.